

# Domain Adaptation of Attention Heads for Zero-shot Anomaly Detection

Kiyeon Jeong<sup>a</sup>, Jaehyuk Heo<sup>b</sup>, Junyeong Son<sup>a</sup>, Pilsung Kang<sup>b,\*</sup>

<sup>a</sup>*Department of Industrial and Management Engineering, Korea University, 145, Anam-Ro, Seongbuk-Gu, Seoul, 02845, Republic of Korea*

<sup>b</sup>*Department of Industrial Engineering, Seoul National University, 1, Gwanak-ro, Gwanak-gu, Seoul, 08826, Republic of Korea*

---

## Abstract

Zero-shot anomaly detection (ZSAD) in images is an approach that can detect anomalies without access to normal samples, which can be beneficial in various realistic scenarios where model training is not possible. However, existing ZSAD research has shown limitations by either not considering domain adaptation of general-purpose backbone models to anomaly detection domains or by implementing only partial adaptation to some model components. In this paper, we propose HeadCLIP to overcome these limitations by effectively adapting both text and image encoders to the domain. HeadCLIP generalizes the concepts of normality and abnormality through learnable prompts in the text encoder, and introduces *learnable head weights* to the image encoder to dynamically adjust the features held by each attention head according to domain characteristics. Additionally, we maximize the effect of domain adaptation by introducing a *joint anomaly score* that utilizes domain-adapted pixel-level information for image-level anomaly detection. Experimental results using multiple real datasets in both industrial and medical domains show that HeadCLIP outperforms existing ZSAD techniques at both pixel and image levels. In the industrial domain, improvements of up to 4.9%p in pixel-level mean anomaly detection score (mAD) and up to 3.0%p in image-level mAD were achieved, with similar improvements (3.2%p,

---

\*Corresponding author. Tel.: +82-2-880-7360

*Email addresses:* [kiyeon\\_jeong@korea.ac.kr](mailto:kiyeon_jeong@korea.ac.kr) (Kiyeon Jeong), [jaehyuk.heo@snu.ac.kr](mailto:jaehyuk.heo@snu.ac.kr) (Jaehyuk Heo), [junyeong\\_son@korea.ac.kr](mailto:junyeong_son@korea.ac.kr) (Junyeong Son), [pilsung\\_kang@snu.ac.kr](mailto:pilsung_kang@snu.ac.kr) (Pilsung Kang)

3.1%p) in the medical domain.

*Keywords:* Image Anomaly Detection, Zero-shot Anomaly Detection, Vision-Language Model

---

## 1. Introduction

Anomaly detection in images plays a crucial role in various real-world applications, including manufacturing inspection (Xie et al., 2024), financial security (Park, 2024), and medical diagnosis (Kumari and Prabha, 2023). In these domains, the ability to detect abnormal cases accurately and efficiently is essential to mitigate potential risks and losses. Unsupervised anomaly detection (UAD) has emerged as a practical approach, as it requires only normal data to learn patterns of typical behavior (Liu et al., 2024a). UAD is particularly useful when anomalous cases are rare, hard to collect, or too diverse to model explicitly.

Despite its strengths, UAD faces critical limitations in scenarios where collecting sufficient normal data is impractical, a challenge commonly referred to as the cold start problem (Cao et al., 2024). For example, in manufacturing, normal data may be unavailable during the early deployment of new processes or equipment (Cao et al., 2024). Similarly, in sensitive domains such as healthcare, privacy and regulatory constraints often restrict the use of patient data for model training (Xie et al., 2024). These conditions hinder the applicability of UAD methods that rely heavily on learning from abundant and representative normal samples (Xie et al., 2024; Kumari and Prabha, 2023; Liu et al., 2024a).

To address these constraints, zero-shot anomaly detection (ZSAD) has recently gained attention. ZSAD leverages the generalization capabilities of pre-trained vision-language models (VLMs), such as CLIP (Radford et al., 2021), enabling anomaly detection in new domains without requiring prior exposure to domain-specific normal data. CLIP, trained on hundreds of millions of image-text pairs from the web (Schuhmann et al., 2022), serves as the foundation for a range of ZSAD methods (Deng et al., 2023; Jeong et al., 2023; Zhou et al., 2024; Cao et al., 2024). These methods detect anomalies by computing the similarity between image features and textual descriptions of normal or abnormal states, using CLIP’s dual encoders.

However, a fundamental challenge remains: CLIP was pre-trained on natural images and internet content, which differ significantly from industrial or

medical images. Industrial data often includes subtle surface-level anomalies (Bergmann et al., 2021), while medical images exhibit domain-specific structures such as tissue textures (Bernal et al., 2015). As a result, effective deployment of CLIP-based ZSAD methods in such domains requires domain adaptation (Hu et al., 2024) of both the image and text encoders.

While prior works attempted various forms of domain alignment, they remain limited. Methods such as AnoVL (Deng et al., 2023) and WinCLIP (Jeong et al., 2023) rely on manually crafted prompts without adapting the encoders. AnomalyCLIP (Zhou et al., 2024) introduces partial adaptation by fine-tuning prompt tokens, while AdaCLIP (Cao et al., 2024) similarly modifies only the textual prompt space. None of these methods sufficiently address the simultaneous and balanced adaptation of both the image and text modalities.

To overcome these limitations, we propose HeadCLIP, a CLIP-based ZSAD framework that enables domain adaptation of both encoders. For the text encoder, HeadCLIP employs learnable text prompts to generalize across normal and abnormal concepts without relying on handcrafted templates. For the image encoder, we introduce learnable head weights (LHW), a novel mechanism that leverages the structure of Vision Transformers (ViTs) (Dosovitskiy et al., 2021). By selectively weighting CLIP’s attention heads, which each capture different visual semantics (Gandelsman et al., 2024), LHW performs domain adaptation while preserving CLIP’s pretrained representational power. Finally, we propose a joint anomaly score (JAS) that integrates pixel-level and image-level anomaly signals, enhancing detection accuracy. Through these contributions, HeadCLIP enables robust, zero-shot anomaly detection in domains where normal data is scarce or inaccessible.

The main contributions of this work are summarized as follows:

- 1) **Learnable Head Weights (LHW)**: We propose a novel domain adaptation method for CLIP’s image encoder by learning attention head weights in Vision Transformers. This approach exploits the head-specific semantic focus to enhance anomaly detection performance in target domains.
- 2) **Joint Anomaly Score (JAS)**: We introduce a scoring strategy that integrates domain-adapted pixel-level and image-level anomaly cues. This method yields robust detection results across a range of anomaly types and JAS weighting configurations.
- 3) **Comprehensive Evaluation**: We validate the proposed framework through extensive experiments on 7 industrial and 10 medical datasets, using mul-

tiple image- and pixel-level evaluation metrics. Our method consistently outperforms state-of-the-art ZSAD approaches.

The remainder of this paper is organized as follows. Section 2 reviews related work on zero-shot anomaly detection and domain adaptation for vision-language models. Section 3 details the proposed HeadCLIP framework, including the design of LHW and JAS. Section 4 presents the experimental setup, results, and analysis. Finally, Section 5 discusses the implications of our findings and outlines future research directions.

## 2. Related works

### 2.1. Anomaly Detection

Anomaly detection aims to identify patterns that deviate significantly from expected behavior or distributions. In industrial settings, image-based anomaly detection enables automated quality control by identifying visual defects on production lines (Yi and Yoon, 2020; Rudolph et al., 2023; Hyun et al., 2024). Similarly, in medical imaging, such techniques have been applied to detect pathological irregularities that may signal disease progression (Zhao et al., 2021; Wang et al., 2021; Kascenas et al., 2022).

The core challenge in anomaly detection lies in the ill-defined and open-ended nature of anomalies: they are often rare, diverse in appearance, and lack a consistent definition (Zhu et al., 2024). These characteristics render supervised approaches impractical in many real-world applications, as collecting and annotating a comprehensive set of anomalies is costly and infeasible (Chiu and Lai, 2023). Consequently, a large body of recent research has focused on unsupervised anomaly detection (UAD) methods, which rely solely on normal data to model typical patterns and identify deviations during inference.

#### 2.1.1. Unsupervised Anomaly Detection

UAD methods operate under the assumption that only normal samples are available during training. At test time, a sample is considered anomalous if it significantly deviates from the learned normal distribution. Broadly, these methods can be categorized into density-based and reconstruction-based approaches.

Density-based methods model the probability distribution of normal data and classify low-likelihood samples as anomalies. These approaches include

(1) normalizing flow-based methods, which estimate exact likelihoods and flag samples with low probabilities as anomalies (Rudolph et al., 2022; Yu et al., 2021) and (2) memory bank-based methods, which store representative normal features and compare them with test samples to compute anomaly scores (Defard et al., 2020; Yi and Yoon, 2020).

Reconstruction-based methods are built on the assumption that models trained to reconstruct normal data will fail to accurately reconstruct anomalies. Anomalies are identified based on discrepancies between the input and its reconstruction. This class of methods has evolved through successive generations of architectures, including autoencoders (Zavrtanik et al., 2021; Chen et al., 2023), generative adversarial networks (GANs) (Yan et al., 2021; Duan et al., 2023), Transformers (You et al., 2022; Yao et al., 2023), and most recently, diffusion models (Zhang et al., 2023a; Mousakhan et al., 2023).

While effective in many cases, these UAD approaches face limitations in domains where acquiring sufficient training data is difficult due to privacy constraints or high data acquisition costs. Furthermore, their performance often degrades when there is a distributional shift between training and testing data (Liu et al., 2024b). These limitations underscore the need for anomaly detection frameworks that offer strong generalization capabilities and can operate under low-data or data-restricted scenarios.

### *2.1.2. Zero-shot Anomaly Detection*

Zero-shot anomaly detection (ZSAD) has emerged as a promising direction for overcoming the limitations of conventional UAD methods, particularly in data-scarce environments. ZSAD methods aim to detect anomalies without requiring normal training samples, by leveraging the zero-shot recognition capabilities of pre-trained vision-language models (VLMs). Among these, CLIP (Radford et al., 2021) has become a key foundation due to its strong generalization abilities, acquired through training on large-scale, diverse image-text pairs.

Early ZSAD approaches, such as AnoVL (Deng et al., 2023), introduced domain-aware state prompting, wherein handcrafted text prompts are used to describe expected anomaly types (see Fig. 1a). While this method injects domain knowledge effectively, it relies heavily on manually crafted prompts and does not adapt well to domains beyond CLIP’s original training data distribution (Zhou et al., 2021).

To alleviate this, AnomalyCLIP (Zhou et al., 2024) proposed partially learnable prompts by introducing trainable tokens that represent normal and

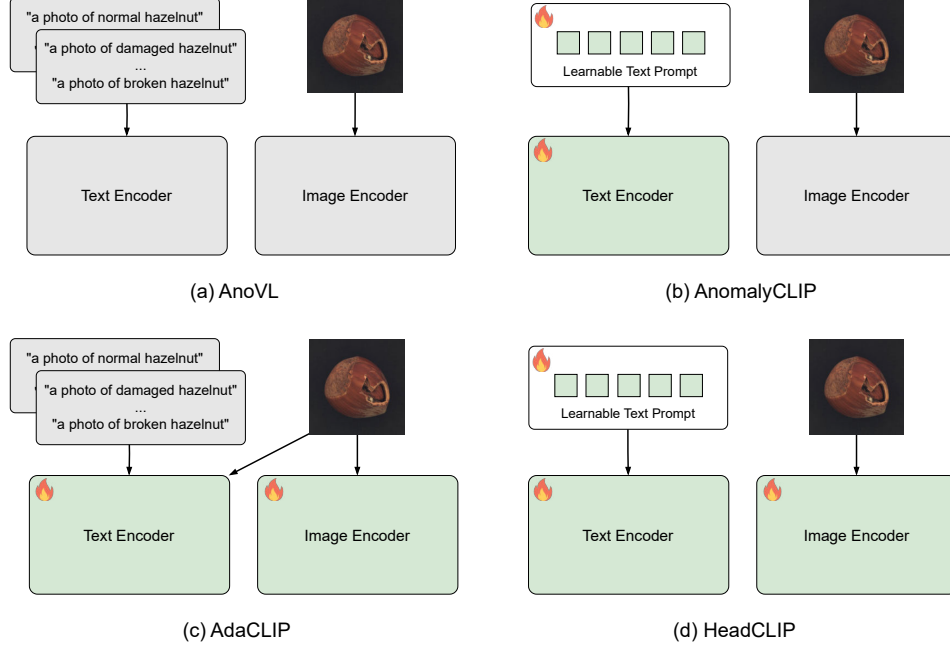


Figure 1: Comparison of domain adaptation approaches in CLIP-based anomaly detection methods: (a) AnoVL, (b) AnomalyCLIP, (c) AdaCLIP, and (d) HeadCLIP. The fire emoji indicates where domain adaptation is performed, with our method achieving more comprehensive adaptation of both modalities.

abnormal concepts (Fig. 1b). Although this enhances the adaptability of the text encoder, the image encoder remains fixed, leading to limited performance when visual domains differ significantly from CLIP’s pretraining corpus.

More recently, AdaCLIP (Cao et al., 2024) extended this direction by enabling partial domain adaptation for both the text and image encoders (Fig. 1c). However, this method still depends on manually defined base prompts, which constrains its generalization to unseen anomaly types and limits flexibility across domains.

To address these challenges, we propose a new strategy that jointly adapts both encoders in a more principled and effective manner. Specifically, we introduce learnable text prompts that represent normal/abnormal semantics without relying on handcrafted tokens, and we propose Learnable Head Weights (LHW) to selectively adapt the image encoder by reweighting the attention heads of the Vision Transformer. Together, these components en-

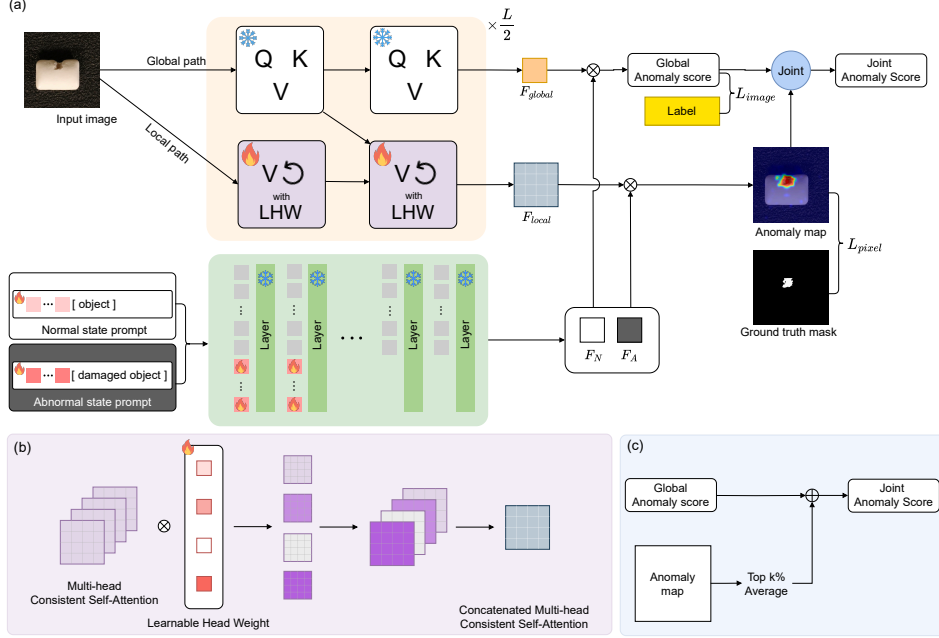


Figure 2: (a) Overview of the proposed anomaly detection framework. The model comprises a global path (top), which employs standard self-attention, and a local path (bottom), which applies consistent self-attention (CSA) enhanced with learnable head weights (LHW) to extract fine-grained features. A text encoder processes both normal and abnormal prompts to guide semantic understanding. The resulting global and local features are fused to produce an anomaly map and a global anomaly score, which are integrated into the Joint Anomaly Score (JAS). (b) Architecture of the multi-head CSA module. Each attention head is modulated by a learnable weight, and the outputs are concatenated to form a unified local representation. (c) Computation of the JAS by combining the global anomaly score with the top- $k\%$  average of the pixel-wise anomaly map.

able robust domain adaptation and significantly enhance zero-shot anomaly detection performance across diverse visual domains.

### 3. Proposed method

#### 3.1. Overview

The overall architecture of the proposed framework, HeadCLIP, is illustrated in Figure 2. Built upon the CLIP backbone, HeadCLIP enhances zero-

shot anomaly detection (ZSAD) by jointly adapting the image and text encoders to the target domain.

For the text encoder, we employ learnable prompt tokens combined with object-independent template structures. This design allows the model to capture general normal and abnormal patterns without requiring class-specific textual descriptions, thereby improving transferability across domains (Zhou et al., 2024).

The image encoder comprises a dual-path architecture: a global path using standard self-attention to extract high-level semantic features, and a local path using consistent self-attention (CSA) modulated by learnable head weights (LHW). The LHW mechanism enables each attention head in the Vision Transformer to specialize in domain-relevant visual cues, thereby improving feature extraction for anomaly localization.

The outputs from the image and text encoders are fused to compute both a global anomaly score and a pixel-wise anomaly map. We further introduce the Joint Anomaly Score (JAS), which integrates these outputs to support robust image-level anomaly detection, benefiting from the fine-grained domain adaptation in the local path.

The detailed components of HeadCLIP are described in Sections 3.2 through 3.4, covering the prompt learning strategy, the LHW-based local path, and the formulation of the joint scoring mechanism.

### 3.2. Text Encoder with Learnable Token

As illustrated in the bottom-left of Figure 2-(a), HeadCLIP’s text encoder is based on object-independent prompt templates, denoted as  $P_{\text{Normal}}$  and  $P_{\text{Abnormal}}$ . These templates represent the concepts of normality and abnormality through base tokens such as "object" and "damaged object". To enhance semantic flexibility, we incorporate learnable prompt tokens into these templates, enabling the model to capture anomaly patterns beyond fixed textual descriptors.

In addition to the main prompt tokens, we introduce auxiliary learnable tokens that are embedded into the input sequence at the initial layers of the text encoder. These tokens are jointly processed with the original tokens through the encoder’s self-attention and feed-forward modules. By restricting their influence to the earlier layers, the model can learn fine-grained, domain-specific semantic features, while preserving the high-level generalization ability encoded in the later layers of the pre-trained CLIP text encoder.



This design is inspired by recent work in anomaly detection (Zhou et al., 2024), and offers key advantages: it avoids reliance on class-specific object names, improves adaptability to diverse domains, and enables generalization to unseen anomaly types. The resulting text embeddings  $F_N$  and  $F_A$  are subsequently used to compute similarities with visual features extracted by the image encoder, serving as the semantic reference for zero-shot anomaly detection.

### 3.3. Image Encoder with Learnable Head Weights

The image encoder in CLIP is built upon a Vision Transformer (ViT) architecture, where each attention head captures distinct aspects of an input image, such as texture, shape, or spatial layout (Gandelsman et al., 2024). While this multi-head structure enables rich representation learning, not all heads contribute equally to anomaly detection tasks. Some may encode domain-irrelevant features, while others capture subtle cues essential for identifying anomalies.

To address this, we propose the Learnable Head Weights (LHW) mechanism, which assigns a trainable importance weight to each attention head. This allows the model to dynamically modulate the contribution of each head based on its relevance to anomaly detection in the target domain. The learned weights enable HeadCLIP to emphasize semantically informative attention heads while suppressing irrelevant or noisy ones, thereby enhancing domain-specific feature extraction.

As illustrated in Figure 2-(a), the image encoder processes input images through two parallel attention streams at each transformer layer: a global path using standard self-attention, and a local path using consistent self-attention (CSA) (Li et al., 2025) modulated by LHW. The global path captures high-level semantic context, while the local path emphasizes fine-grained details critical for detecting subtle anomalies. These two feature streams are later fused to generate both pixel-wise and image-level anomaly scores, as described in Section 3.4.

#### 3.3.1. Global Path with Standard Self-Attention

The global path in HeadCLIP follows the standard multi-head self-attention mechanism to extract high-level semantic features from the input image. For the  $k$ -th attention head in the  $l$ -th transformer layer, the self-attention output

$A_{l,k}$  is computed as:

$$A_{l,k} = \sigma \left( \frac{Q_{l,k} K_{l,k}^T}{\sqrt{d_k}} \right) V_{l,k}, \quad (1)$$

where  $\sigma$  denotes the softmax function, and  $d_k$  is the dimensionality of each key vector.  $Q_{l,k}$ ,  $K_{l,k}$ , and  $V_{l,k}$  represent the query, key, and value matrices for the corresponding head.

The outputs of all attention heads are concatenated and projected using a linear transformation:

$$F_{\text{global}}^l = W_{\text{proj}}^l [A_{l,1}; A_{l,2}; \dots; A_{l,n}], \quad (2)$$

where  $W_{\text{proj}}^l$  is a trainable projection matrix, and  $n$  is the number of heads.

After passing through feed-forward networks and normalization layers, the final-layer cls token representation is extracted as the global feature vector  $F_{\text{global}}$ , which serves as the basis for image-level anomaly scoring.

### 3.3.2. Local Path with CSA and Learnable Head Weights

To complement the global semantic representation, the local path employs Consistent Self-Attention (CSA) (Li et al., 2023), which focuses on fine-grained local details essential for detecting subtle anomalies. Unlike standard self-attention, CSA computes self-similarity among value vectors, omitting query and key matrices. For the  $k$ -th head in the  $l$ -th layer, CSA is defined as:

$$H_{l,k} = \sigma \left( \frac{V_{l,k} V_{l,k}^T}{\sqrt{d_k}} \right) V_{l,k}. \quad (3)$$

To adapt the local feature extraction to the anomaly detection context, we introduce Learnable Head Weights (LHW). Each head is assigned a scalar weight  $w_{l,k}$  that scales its output, allowing the model to learn the relative importance of different heads:

$$\hat{H}l, k = w_{l,k} H_{l,k}. \quad (4)$$

The weighted outputs are then concatenated and linearly projected:

$$F_{\text{local}}^l = W_{\text{proj}}^l [\hat{H}l, 1; \hat{H}l, 2; \dots; \hat{H}l, n]. \quad (5)$$

Finally, local features across all layers are aggregated to form the overall local representation:

$$F_{\text{local}} = \sum_{l=1}^{l_{\text{last}}} F_{\text{local}}^l, \quad (6)$$

where  $l_{\text{last}}$  is the index of the final transformer layer in the local path.

By introducing head-wise, layer-specific weights, the model learns to emphasize the most discriminative visual features for anomaly detection. This adaptive weighting bridges the semantic gap between CLIP’s general-purpose visual representations and the domain-specific requirements of anomaly detection, thereby improving detection accuracy in unfamiliar domains.

### 3.4. Joint Anomaly Score

In CLIP-based ZSAD frameworks, anomaly detection is typically addressed through two independent outputs: an image-level anomaly score derived from the cls token (global path) and a pixel-level anomaly map obtained from patch representations (local path). However, a critical limitation of this design lies in the domain adaptation asymmetry: while our proposed LHW module enhances local features via domain adaptation, the global path remains unadapted, leading to a potential mismatch between the two outputs.

To resolve this issue, we introduce the Joint Anomaly Score (JAS), which integrates both global and local information to provide a unified, domain-adapted image-level score. Specifically, the JAS combines a global anomaly score  $S_{\text{global}}$  based on the cls token from the global path and a local anomaly score  $S_{\text{local}}$  computed by aggregating high-activation regions from the anomaly map produced in the local path.

To obtain  $S_{\text{local}}$ , we average the top- $k\%$  pixel-level scores from the anomaly map  $M_a$  as follows:

$$S_{\text{local}} = \frac{1}{|\mathcal{I}|} \sum_{(j,k) \in \mathcal{I}} M_a^{(j,k)}, \quad (7)$$

where  $\mathcal{I}$  denotes the set of spatial coordinates corresponding to the top- $k\%$  anomaly scores, and  $|\mathcal{I}|$  is its cardinality. By focusing on the most salient regions, this formulation avoids the dilution of anomaly signals due to widespread low responses in predominantly normal images (Zhou et al., 2025).

The final JAS is computed as a weighted combination of the two scores:

$$S_{\text{joint}} = rS_{\text{global}} + (1 - r)S_{\text{local}}, \quad (8)$$

where  $r \in [0, 1]$  is a hyperparameter controlling the relative importance of global versus local contributions.

This integration not only enhances the robustness of image-level anomaly detection but also maximizes the utility of domain-specific adaptations captured by LHW. JAS thus offers a principled framework that unifies coarse-grained semantic understanding with fine-grained localization in a fully zero-shot setting.

### 3.5. Training and Inference

HeadCLIP is trained using a joint objective designed to balance global semantic alignment and local anomaly localization. The total loss integrates both image-level and pixel-level supervision to optimize the model components end-to-end.

For global-level supervision, we define a classification loss  $\mathcal{L}_{\text{global}}$  that encourages high cosine similarity between the global visual embeddings and the corresponding text embeddings for normal and anomalous samples. Specifically, cross-entropy loss is applied over similarity scores computed between the global cls token representation and the learnable text prompts.

For pixel-level supervision, we use a binary annotation mask  $\mathbf{T} \in \mathbb{R}^{H \times W}$  where 1 indicates anomalous regions and 0 denotes normal ones. At each spatial location  $(j, k)$ , we compute the similarity between the visual features and the text embeddings for normal ( $F_N$ ) and abnormal ( $F_A$ ) conditions as follows:

$$\mathcal{N}^{(j,k)} = \text{sim}(F_N, v_i^{p(j,k)}), \mathcal{A}^{(j,k)} = \text{sim}(F_A, v_i^{p(j,k)}), \quad (9)$$

where  $v_i^{p(j,k)}$  represents the patch-level visual embedding at location  $(j, k)$ , and  $\text{sim}(\cdot, \cdot)$  is the cosine similarity function.

To address the class imbalance inherent in anomaly segmentation tasks, we adopt a composite local loss  $\mathcal{L}_{\text{local}}$  that combines focal loss for imbalance sensitivity and dice loss for structural boundary supervision:

$$\mathcal{L}_{\text{local}} = \text{FocalLoss}([\mathcal{N}, \mathcal{A}], \mathbf{T}) + \text{DiceLoss}(\mathcal{N}, \mathbf{1} - \mathbf{T}) + \text{DiceLoss}(\mathcal{A}, \mathbf{T}), \quad (10)$$

where  $\mathbf{1}$  is a matrix of ones with dimensions matching  $\mathbf{T}$ .

The overall training loss is defined as:

$$\mathcal{L}_{\text{total}} = \mathcal{L}_{\text{global}} + \mathcal{L}_{\text{local}}^\ell, \quad (11)$$

where  $\ell$  indicates the transformer layer from which the local features are aggregated. The global text prompts, text encoder, and learnable head weights (LHW) are all jointly optimized through this unified loss.

During inference, image-level anomaly detection is performed using the previously defined Joint Anomaly Score (JAS)  $S_{\text{joint}}$  (see Section 3.4). For pixel-level anomaly localization, we generate the final anomaly map  $M$  by combining the normal and abnormal probability maps:

$$M = G_{\sigma} \left( \text{Up} \left( \frac{1}{2}(\mathbf{1} - \mathcal{N} + \mathcal{A}) \right) \right), \quad (12)$$

where  $\text{Up}(\cdot)$  denotes bilinear interpolation to the original image resolution, and  $G_{\sigma}$  applies Gaussian smoothing with kernel parameter  $\sigma$ . This formulation emphasizes regions that exhibit low similarity to the normal prompt and high similarity to the abnormal prompt, yielding a robust pixel-wise anomaly heatmap.

## 4. Experiments

### 4.1. Experimental Settings

We evaluate the performance of HeadCLIP on 17 publicly available anomaly detection datasets across two domains: industrial inspection and medical imaging.

*Industrial domain.* We employ seven datasets that encompass both object-level and surface-level anomalies:

- Object anomalies: MVTec AD (Bergmann et al., 2021), VisA (Zou et al., 2022), MPDD (Jezek et al., 2021), BTAD (Mishra et al., 2021), and SDD (Tabernik et al., 2020).
- Surface anomalies: DAGM (Wieler and Hahn, 2007) and DTD-Synthetic (Aota et al., 2023).

*Medical domain.* We include ten datasets covering a wide range of pathological conditions, including dermatology, endoscopy, radiology, and infectious diseases: ISIC (Codella et al., 2018), CVC-ClinicDB (Bernal et al., 2015), CVC-ColonDB (Tajbakhsh et al., 2016), Kvasir (Jha et al., 2019), Endo (Hicks et al., 2021), TN3k (Gong et al., 2021), HeadCT (Salehi et al., 2021), BrainMRI (Salehi et al., 2021), Br35H (Hamada, 2020), and COVID-19 (Chowdhury et al., 2020).

*Evaluation metrics.* Following the protocol in (Zhang et al., 2023b), we assess anomaly detection performance at two levels:

- Image-level metrics: AUROC (Area Under the Receiver Operating Characteristic), AP (Average Precision), F1-max (maximum F1-score across thresholds).
- Pixel-level metrics: AUROC, AUPRO (Area Under the Per-Region Overlap Curve) (Bergmann et al., 2020), AP, F1-max, IoU-max (maximum Intersection over Union), which provides order-independent evaluation of localization accuracy (Zhang et al., 2024).

We also report mean Anomaly Detection (mAD) (Zhang et al., 2023b), computed as the average of all relevant metrics per level, to provide a comprehensive and balanced assessment. This multi-metric evaluation strategy ensures that both classification and localization capabilities are thoroughly examined under diverse operational conditions.

#### 4.2. Implementation Details

We adopt the publicly available CLIP backbone (ViT-L/14@336px), keeping all parameters frozen during training except for three components: (1) the learnable head weights (LHW) in the image encoder, (2) the learnable word embeddings appended to the text prompts, and (3) the learnable token embeddings inserted into the early layers of the text encoder.

The detailed configuration is as follows. The number of learnable word embeddings  $E$  is set to 12. Four learnable token embeddings are inserted at each of the first 9 transformer layers in the text encoder, following the default protocol of AnomalyCLIP (Zhou et al., 2024). Consistent Self-Attention (CSA) is applied from layers 5 to 19 of the image encoder. Outputs from all CSA layers are aggregated to form the local representation  $F_{\text{local}}$ . Each attention head within CSA is initialized with a learnable weight  $w = 1$  and optimized throughout training.

We benchmark HeadCLIP against existing zero-shot anomaly detection (ZSAD) approaches, including AnoVL (Deng et al., 2023), AnomalyCLIP (Zhou et al., 2024), and AdaCLIP (Cao et al., 2024). All results are reproduced using the official codebases and default settings provided by the respective authors, ensuring a fair and consistent comparison.

In addition, Two cross-domain experimental protocols are adopted. In industrial pretraining, the model is trained on the VisA dataset and evaluated

on MVTec AD. In generalization testing, the model is trained on MVTec AD and evaluated on all remaining datasets (industrial + medical).

All experiments are conducted using PyTorch 2.2.0 and a single NVIDIA RTX 2080 (12GB) GPU. For datasets with multiple sub-categories, reported scores represent the average performance across subdatasets.

#### 4.3. Zero-shot Anomaly Detection Results

We evaluate the performance of HeadCLIP in zero-shot anomaly detection (ZSAD) across both industrial and medical domains. The results demonstrate that HeadCLIP consistently outperforms prior state-of-the-art methods in both pixel-level and image-level detection tasks.

*Industrial domain.* As summarized in Table 1, HeadCLIP achieves a 4.9%p increase in mean anomaly detection (mAD) for pixel-level detection compared to the previous best-performing methods. The model attains the highest mAD across all seven industrial datasets and achieves the highest average score across six evaluation metrics. Notably:

- Out of 35 evaluation cases ( $7 \text{ datasets} \times 5 \text{ metrics}$ ), HeadCLIP ranks first in 22 and second in 12 cases.
- In image-level detection, it improves mAD by 3.7%p, ranking first in 5 out of 7 datasets and showing the highest average across all four metrics.
- Across 21 image-level evaluation cases ( $7 \times 3$ ), HeadCLIP ranks first in 16 and second in 6 cases.

*Medical domain.* Table 2 presents the pixel-level performance on six medical datasets. HeadCLIP improves overall mAD by 3.2%p, achieving:

- The highest average performance across all six metrics.
- First place in 24 out of 30 evaluation cases ( $6 \text{ datasets} \times 5 \text{ metrics}$ ) and second place in 2 cases.

In image-level detection (Table 3), HeadCLIP similarly achieves a 3.2%p in mAD, ranking the first in 7 out of 12 evaluation cases ( $4 \text{ datasets} \times 3 \text{ metrics}$ ) and the second in 5 cases.

Dataset	Model	Image-level				Pixel-level					
		R	A	F	M	R	P	A	F	I	M
MVTecAD	AnoVL	91.5	96.4	92.8	93.6	88.6	74.6	27.2	32.9	20.4	48.7
	AnomalyCLIP	90.2	95.7	92.2	92.7	89.2	<u>81.9</u>	34.7	<u>37.8</u>	<u>24.6</u>	<u>53.6</u>
	AdaCLIP	<u>92.9</u>	<b>96.9</b>	<u>92.9</u>	<u>94.2</u>	<u>90.3</u>	36.2	<b>43.2</b>	24.7	14.9	41.9
	HeadCLIP	<b>93.2</b>	<u>96.8</u>	<b>93.4</b>	<b>94.5</b>	<b>92.0</b>	<b>82.2</b>	<u>39.9</u>	<b>40.6</b>	<b>26.7</b>	<b>56.3</b>
VisA	AnoVL	76.8	79.4	78.8	78.3	88.2	66.4	10.4	15.4	9.1	37.9
	AnomalyCLIP	80.9	83.9	79.6	81.5	94.0	<u>86.5</u>	20.2	25.7	16.1	<u>48.5</u>
	AdaCLIP	<u>85.4</u>	<b>88.3</b>	<u>83.2</u>	<u>85.6</u>	<u>95.6</u>	48.3	<b>29.1</b>	<b>31.0</b>	<b>19.9</b>	44.8
	HeadCLIP	<b>86.3</b>	<u>88.2</u>	<b>83.4</b>	<b>86.0</b>	<b>95.8</b>	<b>88.8</b>	<u>23.4</u>	<u>30.6</u>	<u>19.1</u>	<b>51.5</b>
MPDD	AnoVL	65.0	<u>71.9</u>	78.3	71.8	65.0	36.4	13.9	15.0	10.6	28.2
	AnomalyCLIP	72.8	<u>79.8</u>	79.3	77.3	<u>96.1</u>	<b>89.8</b>	23.5	28.4	18.0	<u>51.2</u>
	AdaCLIP	<u>76.6</u>	<b>80.5</b>	81.0	<b>79.4</b>	<b>96.4</b>	36.7	<b>31.1</b>	<u>28.6</u>	<b>18.8</b>	42.3
	HeadCLIP	<b>77.4</b>	79.4	<b>81.1</b>	<u>79.3</u>	95.7	<u>87.9</u>	<u>25.9</u>	<b>29.7</b>	<u>18.7</u>	<b>51.6</b>
BTAD	AnoVL	72.0	68.2	69.3	69.8	86.6	51.2	23.4	29.2	18.1	41.7
	AnomalyCLIP	<u>87.1</u>	82.3	79.2	82.8	90.9	<u>67.9</u>	31.2	<u>34.0</u>	<u>22.5</u>	<u>49.3</u>
	AdaCLIP	78.4	<u>89.9</u>	<u>87.9</u>	<u>85.4</u>	92.0	25.8	46.4	27.3	16.0	41.5
	HeadCLIP	<b>94.5</b>	<b>97.2</b>	<b>93.9</b>	<b>95.2</b>	<b>95.6</b>	<b>81.4</b>	<b>47.7</b>	<b>50.9</b>	<b>35.6</b>	<b>62.2</b>
SDD	AnoVL	83.2	76.9	67.2	75.8	<u>86.7</u>	<u>53.6</u>	19.2	27.7	16.1	40.7
	AnomalyCLIP	<b>85.4</b>	<b>80.8</b>	<u>74.0</u>	<b>80.0</b>	82.1	53.0	<u>28.1</u>	<u>35.5</u>	<u>21.6</u>	<u>44.1</u>
	AdaCLIP	75.8	60.7	57.1	64.5	73.9	5.9	21.4	7.0	3.6	26.2
	HeadCLIP	<u>84.6</u>	<u>77.2</u>	<b>74.2</b>	<u>78.7</u>	<b>91.3</b>	<b>65.6</b>	<b>40.7</b>	<b>43.3</b>	<b>27.6</b>	<b>53.7</b>
DAGM	AnoVL	89.9	75.1	72.6	79.2	87.5	69.0	11.9	17.8	10.4	39.3
	AnomalyCLIP	97.4	91.7	89.7	92.9	93.6	<u>87.2</u>	53.1	<u>55.4</u>	<u>40.1</u>	<u>65.9</u>
	AdaCLIP	<u>98.6</u>	<u>94.8</u>	<u>92.6</u>	<u>95.3</u>	<u>95.3</u>	28.6	<b>61.6</b>	27.9	17.3	46.1
	HeadCLIP	<b>99.2</b>	<b>96.9</b>	<b>94.5</b>	<b>96.9</b>	<b>96.2</b>	<b>92.4</b>	<u>61.0</u>	<b>61.0</b>	<b>45.7</b>	<b>71.3</b>
DTD-Synthetic	AnoVL	93.7	96.9	92.7	94.4	96.4	87.0	37.0	40.9	26.3	57.5
	AnomalyCLIP	93.0	96.9	93.6	94.5	<u>98.3</u>	<b>94.3</b>	71.8	<b>67.8</b>	<b>51.8</b>	<u>76.8</u>
	AdaCLIP	<u>96.4</u>	<u>98.3</u>	95.6	<u>96.8</u>	98.3	58.1	<b>76.6</b>	59.4	43.9	67.2
	HeadCLIP	<b>96.9</b>	<b>98.8</b>	<b>95.7</b>	<b>97.1</b>	<b>98.6</b>	94.0	<u>72.6</u>	<u>67.8</u>	<u>51.7</u>	<b>76.9</b>
Average	AnoVL	81.7	80.7	78.8	80.4	85.6	62.6	20.4	25.6	15.8	42.0
	AnomalyCLIP	<u>86.7</u>	<u>87.3</u>	84.0	<u>86.0</u>	<u>92.0</u>	<u>80.1</u>	37.5	<u>40.7</u>	<u>27.8</u>	<u>55.6</u>
	AdaCLIP	86.3	87.1	<u>84.3</u>	85.9	91.7	34.2	<u>44.2</u>	29.4	19.2	44.3
	HeadCLIP	<b>90.3</b>	<b>90.6</b>	<b>88.0</b>	<b>89.7</b>	<b>95.0</b>	<b>84.6</b>	<b>44.5</b>	<b>46.3</b>	<b>32.2</b>	<b>60.5</b>

Table 1: ZSAD performance comparison in industrial domain at image and pixel levels. Best performance shown in bold, second-best underlined. R, P, A, F, I, and M denote AUROC, AUPRO, AP, F1-max, IoU-max, and mAD, respectively.

*Qualitative comparison.* Figure 3 illustrates anomaly localization results. HeadCLIP produces cleaner, more localized anomaly maps with reduced false positives compared to prior approaches, in both industrial and medical settings.

*Analysis.* The superior performance of HeadCLIP can be attributed to two primary design choices: (1) Learnable Head Weights (LHW) enable fine-



Dataset	Model	Pixel-level					
		R	P	A	F	I	M
ISIC	AnoVL	<b>93.3</b>	<b>84.2</b>	<b>84.8</b>	<b>77.4</b>	<b>63.1</b>	<b>80.6</b>
	AnomalyCLIP	<u>90.6</u>	81.5	<u>79.1</u>	<u>72.9</u>	<u>57.3</u>	<u>76.3</u>
	AdaCLIP	88.3	31.0	76.5	44.0	28.2	53.6
	HeadCLIP	90.1	<u>81.7</u>	78.8	72.1	56.4	75.8
CVC-ColonDB	AnoVL	77.9	48.9	21.2	28.9	16.9	38.8
	AnomalyCLIP	<u>81.6</u>	<u>69.1</u>	<u>25.6</u>	<u>34.1</u>	<u>20.6</u>	<u>46.2</u>
	AdaCLIP	80.8	44.9	24.3	27.8	16.1	38.8
	HeadCLIP	<b>83.8</b>	<b>72.8</b>	<b>30.3</b>	<b>37.1</b>	<b>22.8</b>	<b>49.4</b>
CVC-ClinicDB	AnoVL	80.9	53.0	32.7	37.0	22.7	45.3
	AnomalyCLIP	<u>82.5</u>	<u>65.8</u>	31.6	<u>39.3</u>	<u>24.4</u>	<u>48.7</u>
	AdaCLIP	77.0	26.5	27.3	25.9	14.9	34.3
	HeadCLIP	<b>85.6</b>	<b>71.0</b>	<b>38.1</b>	<b>44.2</b>	<b>28.4</b>	<b>53.5</b>
Kvasir	AnoVL	73.4	26.2	32.4	38.8	24.1	39.0
	AnomalyCLIP	<u>79.0</u>	<b>50.5</b>	<u>38.4</u>	<u>45.4</u>	<u>29.4</u>	<u>48.5</u>
	AdaCLIP	76.4	40.1	32.5	33.9	20.4	40.7
	HeadCLIP	<b>82.8</b>	<u>48.0</u>	<b>43.2</b>	<b>50.0</b>	<b>33.3</b>	<b>51.5</b>
Endo	AnoVL	81.1	47.5	38.9	44.7	28.8	48.2
	AnomalyCLIP	<u>82.9</u>	<u>60.2</u>	<u>42.6</u>	<u>47.6</u>	<u>31.2</u>	<u>52.9</u>
	AdaCLIP	81.6	44.2	38.2	38.1	23.5	45.1
	HeadCLIP	<b>86.1</b>	<b>66.8</b>	<b>48.1</b>	<b>52.2</b>	<b>35.3</b>	<b>57.7</b>
TN3K	AnoVL	74.9	39.4	29.0	35.9	21.9	40.2
	AnomalyCLIP	76.8	<u>45.2</u>	38.7	<u>40.5</u>	<u>25.4</u>	<u>45.3</u>
	AdaCLIP	<u>80.6</u>	17.0	<u>42.9</u>	29.2	17.1	37.4
	HeadCLIP	<b>80.9</b>	<b>46.4</b>	<b>44.3</b>	<b>45.9</b>	<b>29.8</b>	<b>49.5</b>
Average	AnoVL	80.3	49.9	39.8	43.8	29.6	48.7
	AnomalyCLIP	<u>82.2</u>	<u>62.1</u>	<u>42.7</u>	<u>46.6</u>	<u>31.4</u>	<u>53.0</u>
	AdaCLIP	80.8	34.0	40.3	33.1	20.0	41.6
	HeadCLIP	<b>84.9</b>	<b>64.4</b>	<b>47.2</b>	<b>50.2</b>	<b>34.3</b>	<b>56.2</b>

Table 2: ZSAD performance comparison in medical domain at pixel level. Best performance shown in bold, second-best underlined. R, P, A, F, I, and M denote AUROC, AUPRO, AP, F1-max, IoU-max, and mAD, respectively.

grained, head-level adaptation of the image encoder to the target domain, resulting in more accurate anomaly localization, and (2) the Joint Anomaly Score (JAS) effectively fuses pixel-level and image-level anomaly evidence, leveraging domain-adapted features from the local path to improve global detection robustness. Due to space limitations, detailed class-wise performance results for each dataset are provided in Appendix. Together, these components contribute to HeadCLIP’s stable and generalizable performance across varied datasets and domains.

Dataset	Model	Image-level			
		R	A	F	M
HeadCT	AnoVL	85.1	84.8	79.0	83.0
	AnomalyCLIP	91.8	91.5	87.9	90.4
	AdaCLIP	<u>94.7</u>	<u>93.7</u>	<u>89.4</u>	<u>92.6</u>
	HeadCLIP	<b>95.3</b>	<b>95.9</b>	<b>91.5</b>	<b>94.2</b>
BrainMRI	AnoVL	85.2	90.4	83.8	86.5
	AnomalyCLIP	92.3	94.1	89.9	92.1
	AdaCLIP	<b>96.5</b>	<b>97.6</b>	<b>94.3</b>	<b>96.1</b>
	HeadCLIP	<u>96.1</u>	<u>96.5</u>	<u>93.8</u>	<u>95.5</u>
Br35H	AnoVL	82.7	83.4	77.4	81.2
	AnomalyCLIP	94.1	94.5	86.9	91.8
	AdaCLIP	<b>98.0</b>	<b>98.1</b>	<u>92.2</u>	<u>96.1</u>
	HeadCLIP	<u>97.9</u>	<u>97.9</u>	<b>93.3</b>	<b>96.4</b>
COVID-19	AnoVL	64.2	44.1	42.4	50.2
	AnomalyCLIP	<u>79.3</u>	<u>53.4</u>	<u>53.6</u>	<u>62.1</u>
	AdaCLIP	70.8	48.4	49.0	56.1
	HeadCLIP	<b>86.5</b>	<b>59.2</b>	<b>56.4</b>	<b>67.3</b>
Average	AnoVL	79.3	75.7	70.6	75.2
	AnomalyCLIP	89.4	83.4	79.6	84.1
	AdaCLIP	<u>90.0</u>	<u>84.5</u>	<u>81.2</u>	<u>85.2</u>
	HeadCLIP	<b>93.9</b>	<b>87.4</b>	<b>83.7</b>	<b>88.4</b>

Table 3: ZSAD performance comparison in medical domain at image level. Best performance shown in bold, second-best underlined. R, A, F, and M denote AUROC, AP, F1-max, and mAD, respectively.

#### 4.4. Learnable Head Weights Analysis

To better understand the operational characteristics and generalization behavior of the proposed Learnable Head Weights (LHW), we conduct a detailed analysis along three dimensions:

- Effectiveness in domain adaptation: We examine whether LHW facilitates adaptation of the image encoder to target domains, and how this contributes to anomaly detection performance.
- Robustness across feature extraction layers: We assess whether LHW yields consistent improvements across various layer combinations used to construct  $F_{\text{local}}$ .
- Sensitivity to initialization (described in the following section): We analyze how different initial values for LHW impact convergence and final performance.

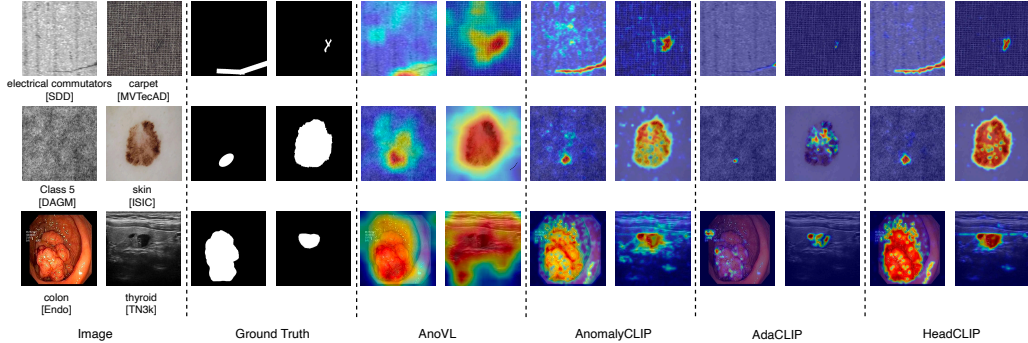


Figure 3: Qualitative comparison of pixel-level anomaly detection results across different models. The leftmost column shows original input images from various domains, along with their corresponding ground truth masks. The comparison demonstrates that HeadCLIP achieves more precise anomaly localization and generates clearer anomaly maps compared to previous methods. These results validate the effectiveness of our method in achieving robust anomaly detection across diverse domains.

These analyses provide insight into the underlying mechanisms of LHW and inform its optimal configuration.

#### 4.4.1. Learnable Head Weights Ablation

We first validate the domain adaptation capability of LHW by comparing performance with and without LHW across pixel-level and image-level detection tasks. In the industrial domain, as shown in Table 4, LHW leads to a 2.2%p improvement in pixel-level mAD, with 88.6% (31 out of 35) of evaluation cases showing performance gains. Similarly, in the medical domain, Table 5 reports a 0.8%p increase in mAD, with 80% (24 out of 30) of cases improving.

Image-level detection results further reinforce LHW’s effectiveness. In the industrial domain, LHW yields consistent mAD gains across all datasets. In the medical domain (Table 6), performance improves across all datasets and all evaluation metrics. Notably, LHW is not directly involved in image-level score computation, but its domain adaptation effects appear to influence the shared text embedding through gradient flow from the anomaly map. This observation suggests that LHW contributes not only to local feature alignment but also enhances global semantic understanding, resulting in improved performance at both levels.

Dataset	LHW	Image-level				Pixel-level					
		R	A	F	M	R	P	A	F	I	M
MVTecAD		<b>90.7</b>	95.6	<b>92.4</b>	<b>92.9</b>	90.5	81.8	32.4	36.0	23.4	52.8
	✓	90.5	95.6	92.1	92.7	<b>92.0</b>	<b>82.2</b>	<b>39.9</b>	<b>40.6</b>	<b>26.7</b>	<b>56.3</b>
VisA		82.2	84.9	81.1	82.7	95.4	86.9	20.1	27.2	16.9	49.3
	✓	<b>82.5</b>	<b>85.2</b>	<b>81.6</b>	<b>83.1</b>	<b>95.8</b>	<b>88.8</b>	<b>23.4</b>	<b>30.6</b>	<b>19.1</b>	<b>51.5</b>
MPDD		<b>76.0</b>	<b>78.9</b>	<b>79.5</b>	<b>78.1</b>	95.1	86.4	25.1	28.4	17.9	50.6
	✓	74.9	77.5	79.0	77.1	<b>95.7</b>	<b>87.9</b>	<b>25.9</b>	<b>29.7</b>	<b>18.7</b>	<b>51.6</b>
BTAD		92.7	93.7	89.4	91.9	95.5	81.0	<b>50.0</b>	<b>52.2</b>	<b>36.1</b>	<b>63.0</b>
	✓	<b>92.9</b>	<b>94.8</b>	<b>90.0</b>	<b>92.6</b>	<b>95.6</b>	<b>81.4</b>	47.7	50.9	35.6	62.2
SDD		86.3	83.6	77.0	82.3	89.1	<b>65.7</b>	28.8	37.1	22.8	48.7
	✓	<b>87.0</b>	<b>84.8</b>	<b>80.3</b>	<b>84.1</b>	<b>91.3</b>	65.6	<b>40.7</b>	<b>43.3</b>	<b>27.6</b>	<b>53.7</b>
DAGM		97.7	92.6	<b>91.2</b>	93.8	95.5	91.5	58.0	59.5	44.0	69.7
	✓	<b>97.8</b>	<b>92.7</b>	91.2	<b>93.9</b>	<b>96.2</b>	<b>92.4</b>	<b>61.0</b>	<b>61.0</b>	<b>45.7</b>	<b>71.3</b>
DTD-Synthetic		<b>93.5</b>	<b>96.9</b>	<b>93.7</b>	<b>94.7</b>	98.0	93.5	66.7	64.9	48.4	74.3
	✓	93.4	96.8	93.5	94.6	<b>98.6</b>	<b>94.1</b>	<b>72.6</b>	<b>67.8</b>	<b>51.7</b>	<b>76.9</b>
Average		<b>88.4</b>	89.5	86.3	88.1	94.2	83.8	40.1	43.6	29.9	58.3
	✓	88.4	<b>89.6</b>	<b>86.8</b>	<b>88.3</b>	<b>95.0</b>	<b>84.6</b>	<b>44.5</b>	<b>46.3</b>	<b>32.2</b>	<b>60.5</b>

Table 4: Ablation study results of LHW in industrial domain at image and pixel levels without JAS. Higher performance shown in bold. R, P, A, F, I, and M denote AUROC, AUPRO, AP, F1-max, IoU-max, and mAD, respectively.

#### 4.4.2. Learnable Head Weights Across Local Feature Extraction Settings

We next investigate whether the effectiveness of LHW depends on the choice of transformer layers used for local feature extraction. Multiple configurations are tested by varying the layers from which  $F_{\text{local}}$  is aggregated.

In the industrial domain, LHW consistently improves image-level mAD in all seven layer configurations, with gains ranging from 0.2 to 1.7%p. Pixel-level performance also improves in most configurations. A similar pattern is observed in the medical domain, where LHW yields image-level improvements of 1.3 to 4.2%p and pixel-level improvements of 0.4 to 3.4%p across different settings.

These results demonstrate that the proposed LHW module contributes robustly across diverse architectural configurations, further validating its general applicability for anomaly detection in varying domain scenarios.

#### 4.4.3. Learnable Head Weights Initialization Value Ablation

To evaluate the sensitivity of LHW to different initialization strategies, we compare the effects of Gaussian and uniform initialization methods on

Dataset	LHW	Pixel-Level					
		R	P	A	F	I	M
ISIC		88.8	80.0	76.6	70.9	54.9	74.3
	✓	<b>90.1</b>	<b>81.7</b>	<b>78.8</b>	<b>72.1</b>	<b>56.4</b>	<b>75.8</b>
CVC-ColonDB		83.7	<b>72.8</b>	<b>31.6</b>	<b>37.8</b>	<b>23.3</b>	<b>49.8</b>
	✓	<b>83.8</b>	72.8	30.3	37.1	22.8	49.4
CVC-ClinicDB		84.9	70.3	37.7	44.1	28.3	53.1
	✓	<b>85.6</b>	<b>71.0</b>	<b>38.1</b>	<b>44.2</b>	<b>28.4</b>	<b>53.5</b>
Kvasir		82.0	47.4	42.6	49.9	33.2	51.0
	✓	<b>82.8</b>	<b>48.0</b>	<b>43.2</b>	<b>50.0</b>	<b>33.3</b>	<b>51.5</b>
Endo		85.8	66.5	48.0	<b>52.7</b>	<b>35.8</b>	<b>57.7</b>
	✓	<b>86.1</b>	<b>66.8</b>	<b>48.1</b>	52.2	35.3	57.7
TN3K		77.9	44.4	40.8	43.4	27.7	46.8
	✓	<b>80.9</b>	<b>46.4</b>	<b>44.3</b>	<b>45.9</b>	<b>29.8</b>	<b>49.5</b>
Average		83.8	63.6	46.2	49.8	33.9	55.5
	✓	<b>84.9</b>	<b>64.4</b>	<b>47.2</b>	<b>50.2</b>	<b>34.3</b>	<b>56.2</b>

Table 5: Ablation study results of LHW in medical domain at pixel level without JAS. Higher performance shown in bold. R, P, A, F, I, and M denote AUROC, AUPRO, AP, F1-max, IoU-max, and mAD, respectively.

Dataset	LHW	Image-Level			
		R	A	F	M
HeadCT		92.9	92.3	89.4	91.6
	✓	<b>93.5</b>	<b>93.1</b>	<b>90.1</b>	<b>92.2</b>
BrainMRI		93.0	94.3	90.7	92.7
	✓	<b>93.0</b>	<b>94.4</b>	<b>91.8</b>	<b>93.1</b>
Br35h		95.3	95.4	88.2	93.0
	✓	<b>95.7</b>	<b>95.7</b>	<b>89.8</b>	<b>93.7</b>
COVID-19		79.5	<b>57.0</b>	<b>56.0</b>	64.2
	✓	<b>80.7</b>	56.9	55.1	<b>64.2</b>
Average		90.2	84.8	81.1	85.4
	✓	<b>90.7</b>	<b>85.0</b>	<b>81.7</b>	<b>85.8</b>

Table 6: Ablation study results of LHW in medical domain at image level without JAS. Higher performance shown in bold. R, A, F, and M denote AUROC, AP, F1-max, and mAD, respectively.

pixel-level anomaly detection performance. Table 8 summarizes the results across both industrial and medical domains.

*Gaussian initialization.* When LHW is initialized with Gaussian-distributed random values, performance significantly deteriorates—achieving 59.6% mAD

Layer Index	LHW	Industrial		Medical	
		Image	Pixel	Image	Pixel
6, 12, 18, 24		86.0	<b>84.1</b>	<b>55.6</b>	53.0
	✓	<b>87.7</b>	84.0	54.8	<b>54.8</b>
12, 18, 24		<b>86.9</b>	<b>84.2</b>	58.3	53.4
	✓	86.7	83.1	<b>58.7</b>	<b>54.7</b>
18, 24		87.6	84.9	59.5	52.9
	✓	<b>87.8</b>	<b>85.3</b>	<b>60.8</b>	<b>54.9</b>
24		87.9	86.1	58.4	54.0
	✓	<b>88.1</b>	<b>86.2</b>	<b>60.3</b>	<b>57.4</b>
18		87.8	<b>86.0</b>	57.3	50.3
	✓	<b>88.0</b>	85.4	<b>59.7</b>	<b>52.9</b>
12		86.8	<b>83.7</b>	45.0	49.8
	✓	<b>86.9</b>	83.1	<b>49.2</b>	<b>52.0</b>
6		86.6	89.1	32.3	47.7
	✓	<b>86.8</b>	<b>90.2</b>	<b>34.1</b>	<b>48.1</b>

Table 7: Ablation study results of LHW under different local feature extraction settings, showing average mAD of HeadCLIP without JAS in industrial and medical domains. Each setting corresponds to the use of  $F_{local}$ , obtained by aggregating features from the specified layers in the image encoder’s local path. Higher performance is shown in bold

in the industrial domain and 54.5% in the medical domain. This result suggests that random initial weights fail to reflect the functional characteristics of individual attention heads, leading to suboptimal or unstable domain adaptation during training.

*Uniform initialization.* We further investigate uniform initializations with values of 0.0, 0.5, and 1.0. A gradual improvement is observed as the initialization value increases. In the industrial domain, pixel-level performance rises from 60.1% (init=0.0) to 60.5% (init=1.0). In the medical domain, performance improves from 54.6% to 56.2% across the same initialization range.

These results indicate that initializing LHW with uniform values closer to 1.0, which maintains balanced attention contribution at the start of training, facilitates more effective learning. In contrast, assigning arbitrary or near-zero weights appears to hinder the model’s ability to leverage the expressive power of individual heads, especially in early training stages.

Initialization	Pixel-level	
	Industrial	Medical
Gaussian	59.6	54.5
0.0	60.1	54.6
0.5	<u>60.4</u>	<u>55.8</u>
1.0	<b>60.5</b>	<b>56.2</b>

Table 8: Ablation study results of initialization value of LHW, showing average mAD of HeadCLIP in industrial and medical domains. Best performance shown in bold, second-best underlined.

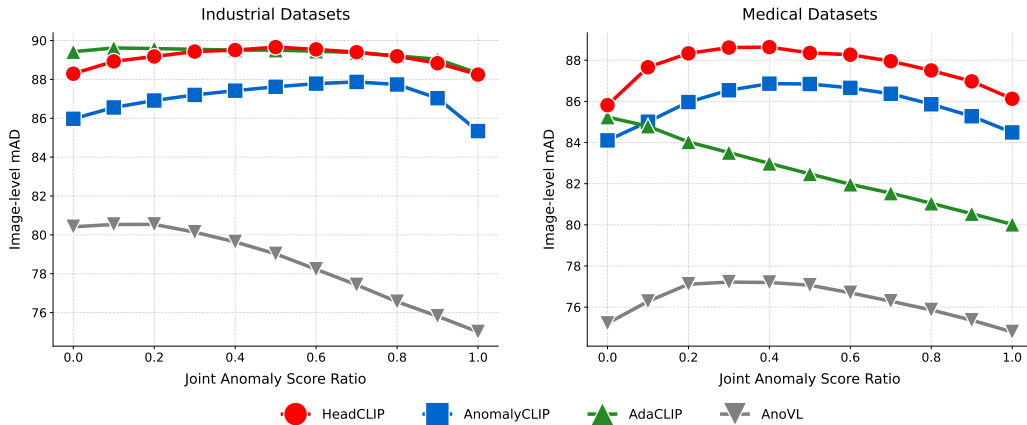


Figure 4: Image-level mean anomaly detection (mAD) performance as a function of the joint anomaly score ratio (x-axis) on industrial (left) and medical (right) datasets. The plots compare four methods with the y-axis showing image-level mAD. The results illustrate how varying the joint anomaly score ratio influences the overall detection performance for each approach.

#### 4.5. Ablation Study

##### 4.5.1. Joint Anomaly Score Ablation

To evaluate the effectiveness and robustness of the proposed Joint Anomaly Score (JAS), we conduct ablation experiments by varying the score ratio parameter  $r$ , which controls the relative contribution of global and local anomaly scores. Figure 4 presents the results across datasets in both industrial and medical domains.

The proposed HeadCLIP framework consistently outperforms existing methods across a wide range of  $r$  values. In particular, in the medical domain, HeadCLIP maintains the highest mean anomaly detection (mAD) per-

formance across all tested ratio values. In the industrial domain, it achieves either the top or near-top performance in most configurations, indicating its robustness to changes in the score fusion strategy.

Among baseline methods, AnomalyCLIP exhibits relatively stable performance across different ratio values but underperforms HeadCLIP consistently. AdaCLIP shows a notable performance decline as  $r$  increases in the medical domain, suggesting poor integration of global-local cues when domain adaptation is suboptimal. AnoVL, which lacks an explicit domain adaptation mechanism, yields the lowest performance in both domains regardless of ratio value.

These findings suggest that JAS is most effective when built upon strong domain-adapted features from both modalities. Moreover, HeadCLIP demonstrates high robustness to the joint score ratio, maintaining stable and superior detection performance across varying fusion strategies and domain characteristics.

#### 4.5.2. Module Ablation

To assess the individual and combined contributions of the two core components, Learnable Head Weights (LHW) and the Joint Anomaly Score (JAS), we conduct a module-wise ablation study. Table 9 summarizes the performance changes when each module is removed from the full HeadCLIP model.

*Impact of removing JAS.* Removing JAS leads to a noticeable decline in image-level anomaly detection performance, with a decrease of 1.4%p in the industrial domain and 2.6%p in the medical domain. This highlights the importance of leveraging pixel-level domain-adapted features to enhance global anomaly scoring.

*Impact of removing both JAS and LHW.* When LHW is additionally removed, a further degradation is observed, particularly in pixel-level performance. Specifically, mAD drops by 2.2%p in the industrial domain and 0.7%p in the medical domain. This indicates that LHW plays a key role in improving anomaly localization by enabling per-head visual adaptation to domain-specific characteristics.

*Summary.* The best performance across both image-level and pixel-level detection is achieved when both LHW and JAS are included, confirming that



Model	LHW	JAS	Image-level		Pixel-level	
			Industrial	Medical	Industrial	Medical
HeadCLIP	✓	✓	89.7	88.4	60.5	56.2
	✓		88.3(-1.4)	85.8(-2.6)	60.5	56.2
			88.1(-0.2)	85.4(-0.4)	58.3(-2.2)	55.5(-0.7)

Table 9: Component ablation study results of LHW and JAS, showing average mAD in industrial and medical domains at both image and pixel levels. Numbers in parentheses indicate the difference in percentage points (%p).

these modules contribute complementary capabilities: LHW enhances fine-grained visual representation, while JAS enables robust score fusion across modalities and scales. Their joint application leads to consistent performance gains in both domains.

## 5. Conclusion

This paper presents HeadCLIP, a novel zero-shot anomaly detection (ZSAD) framework that incorporates domain-specific adaptation mechanisms for both image and text encoders. To address the limitations of existing ZSAD methods in handling domain discrepancies, HeadCLIP introduces two key components: (1) Learnable Head Weights (LHW) for attention-based visual adaptation and (2) a Joint Anomaly Score (JAS) that integrates pixel-level and image-level anomaly evidence.

Extensive experiments across industrial and medical datasets demonstrate the superiority of the proposed framework. HeadCLIP outperforms prior methods such as AnoVL, AnomalyCLIP, and AdaCLIP by up to 4.9 percentage points in pixel-level mAD and 3.2%p in image-level mAD. These improvements are consistently observed across multiple datasets and evaluation metrics.

Ablation studies further validate the individual contributions of each component: LHW enables the image encoder to capture domain-relevant features through head-wise weighting, while JAS enhances robustness and discriminative power in image-level detection by effectively combining multi-scale anomaly cues.

Beyond its empirical performance, HeadCLIP offers a practical solution for domains where normal data is scarce or unavailable, such as in early-stage industrial inspection and privacy-sensitive medical diagnosis. The proposed approach advances the field of ZSAD by introducing a modality-aware,

domain-adaptive architecture that remains effective without supervised normal training data.

Future research may explore the extension of this framework to broader multi-modal contexts and the integration with open-set or incremental learning paradigms, further enhancing its adaptability and generalization capacity across real-world anomaly detection scenarios.

## References

- Aota, T., Tong, L.T.T., Okatani, T., 2023. Zero-shot versus many-shot: Unsupervised texture anomaly detection, in: *Proceedings of the IEEE/CVF Winter Conference on Applications of Computer Vision*, pp. 5553–5561.
- Bergmann, P., Batzner, K., Fauser, M., Sattlegger, D., Steger, C., 2021. The mvtec anomaly detection dataset: A comprehensive real-world dataset for unsupervised anomaly detection. *Journal of Vision* 129, 1038–1059.
- Bergmann, P., Fauser, M., Sattlegger, D., Steger, C., 2020. Uninformed students: Student-teacher anomaly detection with discriminative latent embeddings, in: *Proceedings of the IEEE/CVF Conference on Computer Vision and Pattern Recognition*, pp. 4182–4191.
- Bernal, J., Sánchez, F.J., Fernández-Esparrach, G., Gil, D., de Miguel, C.R., Vilariño, F., 2015. WM-DOVA maps for accurate polyp highlighting in colonoscopy: Validation vs. saliency maps from physicians. *Computerized Medical Imaging and Graphics* 43, 99–111.
- Cao, Y., Zhang, J., Frittoli, L., Cheng, Y., Shen, W., Boracchi, G., 2024. Ada-clip: Adapting clip with hybrid learnable prompts for zero-shot anomaly detection, in: *Proceedings of the European Conference on Computer Vision*, pp. 55–72.
- Chen, R., Xie, G., Liu, J., Wang, J., Luo, Z., Wang, J., Zheng, F., 2023. Easynet: An easy network for 3d industrial anomaly detection, in: *Proceedings of the ACM International Conference on Multimedia*, pp. 7038–7046.
- Chiu, L.L., Lai, S.H., 2023. Self-supervised normalizing flows for image anomaly detection and localization, in: *Proceedings of the IEEE/CVF Conference on Computer Vision and Pattern Recognition*, pp. 2927–2936.

- Chowdhury, M.E.H., Rahman, T., Khandakar, A., Mazhar, R., Abdul Kadir, M., Bin Mahbub, Z., Reajul Islam, K., Salman Khan, M., Iqbal, A., Al-Emadi, N., Bin Ibne Reaz, M., Tariqul Islam, M., 2020. Can ai help in screening viral and covid-19 pneumonia? *IEEE Access* 8, 132665–132676.
- Codella, N.C.F., Gutman, D.A., Celebi, M.E., Helba, B., Marchetti, M.A., Dusza, S.W., Kalloo, A., Liopyris, K., Mishra, N.K., Kittler, H., Halpern, A., 2018. Skin lesion analysis toward melanoma detection: A challenge at the 2017 international symposium on biomedical imaging (isbi), hosted by the international skin imaging collaboration (isic), in: *IEEE International Symposium on Biomedical Imaging*, pp. 168–172.
- Defard, T., Setkov, A., Loesch, A., Audigier, R., 2020. Padim: A patch distribution modeling framework for anomaly detection and localization, in: *Pattern Recognition. ICPR International Workshops and Challenges*, pp. 475–489.
- Deng, H., Zhang, Z., Bao, J., Li, X., 2023. Anovl: Adapting vision-language models for unified zero-shot anomaly localization. *arXiv preprint arXiv:2308.15939* .
- Dosovitskiy, A., Beyer, L., Kolesnikov, A., Weissenborn, D., Zhai, X., Unterthiner, T., Dehghani, M., Minderer, M., Heigold, G., Gelly, S., Uszkoreit, J., Houlsby, N., 2021. An image is worth 16x16 words: Transformers for image recognition at scale, in: *Proceedings of the International Conference on Learning Representations*.
- Duan, Y., Hong, Y., Niu, L., Zhang, L., 2023. Few-shot defect image generation via defect-aware feature manipulation, in: *Proceedings of the AAAI Conference on Artificial Intelligence*, pp. 571–578.
- Gandelsman, Y., Efros, A.A., Steinhardt, J., 2024. Interpreting clip’s image representation via text-based decomposition, in: *Proceedings of the International Conference on Learning Representations*.
- Gong, H., Chen, G., Wang, R., Xie, X., Mao, M., Yu, Y., Chen, F., Li, G., 2021. Multi-task learning for thyroid nodule segmentation with thyroid region prior, in: *IEEE International Symposium on Biomedical Imaging*, pp. 257–261.

- Hamada, A., 2020. Br35h :: Brain tumor detection 2020. <https://www.kaggle.com/datasets/ahmedhamada0/brain-tumor-detection>. Kaggle.
- Hicks, S.A., Jha, D., Thambawita, V., Halvorsen, P., Hammer, H.L., Riegler, M.A., 2021. The endotect 2020 challenge: Evaluation and comparison of classification, segmentation and inference time for endoscopy, in: Pattern Recognition. ICPR International Workshops and Challenges, pp. 263–274.
- Hu, X., Zhang, K., Xia, L., Chen, A., Luo, J., Sun, Y., Wang, K., Qiao, N., Zeng, X., Sun, M., Kuo, C., Nevatia, R., 2024. Reclip: Refine contrastive language image pre-training with source free domain adaptation, in: Proceedings of the IEEE/CVF Winter Conference on Applications of Computer Vision, pp. 2982–2991.
- Hyun, J., Kim, S., Jeon, G., Kim, S.H., Bae, K., Kang, B.J., 2024. Reconpatch: Contrastive patch representation learning for industrial anomaly detection, in: Proceedings of the IEEE/CVF Winter Conference on Applications of Computer Vision, pp. 2041–2050.
- Jeong, J., Zou, Y., Kim, T., Zhang, D., Ravichandran, A., Dabeer, O., 2023. Winclip: Zero-/few-shot anomaly classification and segmentation. Proceedings of the IEEE/CVF Conference on Computer Vision and Pattern Recognition , 19606–19616.
- Jezek, S., Jonak, M., Burget, R., Dvorak, P., Skotak, M., 2021. Deep learning-based defect detection of metal parts: Evaluating current methods in complex conditions, in: International Congress on Ultra Modern Telecommunications and Control Systems and Workshops, pp. 66–71.
- Jha, D., Smedsrud, P.H., Riegler, M., Halvorsen, P., de Lange, T., Johansen, D., Johansen, H.D., 2019. Kvasir-seg: A segmented polyp dataset, in: Conference on Multimedia Modeling, pp. 451–462.
- Kascenas, A., Pugeault, N., O’Neil, A.Q., 2022. Denoising autoencoders for unsupervised anomaly detection in brain mri, in: International Conference on Medical Imaging with Deep Learning, pp. 653–664.
- Kumari, S., Prabha, C., 2023. A comprehensive review on anomaly detection in images: Challenges and future research directions, in: IEEE North Karnataka Subsection Flagship International Conference.

- Li, Y., Wang, H., Duan, Y., Li, X., 2023. Clip surgery for better explainability with enhancement in open-vocabulary tasks. arXiv preprint arXiv:2304.05653 .
- Li, Y., Wang, H., Duan, Y., Zhang, J., Li, X., 2025. A closer look at the explainability of contrastive language-image pre-training. Pattern Recognition 162, 111409.
- Liu, J., Xie, G., Wang, J., Li, S., Wang, C., Zheng, F., Jin, Y., 2024a. Deep industrial image anomaly detection: A survey. Machine Intelligence Research 21, 104–135.
- Liu, Z., Zhou, Y., Xu, Y., Wang, Z., 2024b. Simplenet: A simple network for image anomaly detection and localization. arXiv preprint arXiv:2303.15140 .
- Mishra, P., Verk, R., Fornasier, D., Piciarelli, C., Foresti, G.L., 2021. VT-ADL: a vision transformer network for image anomaly detection and localization, in: IEEE International Symposium on Industrial Electronics, pp. 1–6.
- Mousakhan, A., Brox, T., Tayyub, J., 2023. Anomaly detection with conditioned denoising diffusion models. arXiv preprint arXiv:2305.15956 .
- Park, T., 2024. Enhancing anomaly detection in financial markets with an llm-based multi-agent framework. arXiv preprint arXiv:2403.19735 .
- Radford, A., Kim, J.W., Hallacy, C., Ramesh, A., Goh, G., Agarwal, S., Sastry, G., Askell, A., Mishkin, P., Clark, J., Krueger, G., Sutskever, I., 2021. Learning transferable visual models from natural language supervision, in: Proceedings of the International Conference on Machine Learning, pp. 8748–8763.
- Rudolph, M., Wehrbein, T., Rosenhahn, B., Wandt, B., 2022. Fully convolutional cross-scale-flows for image-based defect detection, in: Proceedings of the IEEE/CVF Winter Conference on Applications of Computer Vision, pp. 1829–1838.
- Rudolph, M., Wehrbein, T., Rosenhahn, B., Wandt, B., 2023. Asymmetric student-teacher networks for industrial anomaly detection, in: Proceedings

- of the IEEE/CVF Winter Conference on Applications of Computer Vision, pp. 2591–2601.
- Salehi, M., Sadjadi, N., Baselizadeh, S., Rohban, M.H., Rabiee, H.R., 2021. Multiresolution knowledge distillation for anomaly detection, in: Proceedings of the IEEE/CVF Conference on Computer Vision and Pattern Recognition, pp. 14902–14912.
- Schuhmann, C., Beaumont, R., Vencu, R., Gordon, C., Wightman, R., Cherti, M., Coombes, T., Katta, A., Mullis, C., Wortsman, M., Schramowski, P., Kundurthy, S., Crowson, K., Schmidt, L., Kaczmarczyk, R., Jitsev, J., 2022. LAION-5B: an open large-scale dataset for training next generation image-text models, in: Advances in Neural Information Processing Systems.
- Tabernik, D., Sela, S., Skvarc, J., Skocaj, D., 2020. Segmentation-based deep-learning approach for surface-defect detection. *Journal of Intelligence Manufacturing* 31, 759–776.
- Tajbakhsh, N., Gurudu, S.R., Liang, J., 2016. Automated polyp detection in colonoscopy videos using shape and context information. *IEEE Transactions on Medical Imaging* 35, 630–644.
- Wang, J., Li, W., Chen, Y., Fang, W., Kong, W., He, Y., Shi, G., 2021. Weakly supervised anomaly segmentation in retinal oct images using an adversarial learning approach. *Biomedical Optics Express* .
- Wieler, M., Hahn, T., 2007. Weakly supervised learning for industrial optical inspection, in: DAGM Symposium.
- Xie, G., Wang, J., Liu, J., Lyu, J., Liu, Y., Wang, C., Zheng, F., Jin, Y., 2024. Im-iad: Industrial image anomaly detection benchmark in manufacturing. *IEEE Transactions on Cybernetics* 54, 2720–2733.
- Yan, X., Zhang, H., Xu, X., Hu, X., Heng, P., 2021. Learning semantic context from normal samples for unsupervised anomaly detection, in: Proceedings of the AAAI Conference on Artificial Intelligence, pp. 3110–3118.
- Yao, X., Li, R., Qian, Z., Luo, Y., Zhang, C., 2023. Focus the discrepancy: Intra- and inter-correlation learning for image anomaly detection, in: Proceedings of the IEEE/CVF International Conference on Computer Vision, pp. 6780–6790.

- Yi, J., Yoon, S., 2020. Patch svdd: Patch-level svdd for anomaly detection and segmentation, in: Proceedings of the Asian Conference on Computer Vision, pp. 375–390.
- You, Z., Cui, L., Shen, Y., Yang, K., Lu, X., Zheng, Y., Le, X., 2022. A unified model for multi-class anomaly detection. *Advances in Neural Information Processing Systems* .
- Yu, J., Zheng, Y., Wang, X., Li, W., Wu, Y., Zhao, R., Wu, L., 2021. Fastflow: Unsupervised anomaly detection and localization via 2d normalizing flows. *arXiv preprint arXiv:2111.07677* .
- Zavrtanik, V., Kristan, M., Skocaj, D., 2021. Dræm – a discriminatively trained reconstruction embedding for surface anomaly detection, in: Proceedings of the IEEE/CVF International Conference on Computer Vision, pp. 8310–8319.
- Zhang, H., Wang, Z., Wu, Z., Jiang, Y.G., 2023a. Diffusionad: Norm-guided one-step denoising diffusion for anomaly detection. *arXiv preprint arXiv:2303.08730* .
- Zhang, J., Chen, X., Wang, Y., Wang, C., Liu, Y., Li, X., Yang, M.H., Tao, D., 2023b. Exploring plain vit reconstruction for multi-class unsupervised anomaly detection. *arXiv preprint arXiv:2312.07495* .
- Zhang, J., Wang, C., Li, X., Tian, G., Xue, Z., Liu, Y., Pang, G., Tao, D., 2024. Learning feature inversion for multi-class anomaly detection under general-purpose coco-ad benchmark. *arXiv preprint arXiv:2404.10760* .
- Zhao, H., Li, Y., He, N., Ma, K., Fang, L., Li, H., Zheng, Y., 2021. Anomaly detection for medical images using self-supervised and translation-consistent features. *IEEE Transactions on Medical Imaging* 40, 3641–3651.
- Zhou, K., Yang, J., Loy, C.C., Liu, Z., 2021. Learning to prompt for vision-language models. *arXiv preprint arXiv:2109.01134* .
- Zhou, Q., Pang, G., Tian, Y., He, S., Chen, J., 2024. Anomalyclip: Object-agnostic prompt learning for zero-shot anomaly detection, in: Proceedings of the International Conference on Learning Representations.

- Zhou, Y., Xu, X., Song, J., Shen, F., Shen, H.T., 2025. Msflow: Multiscale flow-based framework for unsupervised anomaly detection. *IEEE Transactions on Neural Networks and Learning Systems* 36, 2437–2450.
- Zhu, J., Ding, C., Tian, Y., Pang, G., 2024. Anomaly heterogeneity learning for open-set supervised anomaly detection, in: *Proceedings of the IEEE/CVF Conference on Computer Vision and Pattern Recognition*, pp. 17616–17626.
- Zou, Y., Jeong, J., Pemula, L., Zhang, D., Dabeer, O., 2022. Spot-the-difference self-supervised pre-training for anomaly detection and segmentation, in: *Proceedings of the European Conference on Computer Vision*, pp. 392–408.



## 6. Appendix

This appendix presents detailed subclass-level results for each dataset used in our experiments, shown in Tables 10 through 26. We report performance metrics at both image and pixel levels to provide a more granular view of HeadCLIP’s performance across different anomaly types. These results offer additional insights into the model’s effectiveness and consistency across diverse domains.

Subclass	Model	Image-level			Pixel-level				
		R	A	F	R	P	A	F	I
bottle	AnoVL	<b>97.5</b>	<b>99.3</b>	<b>96.8</b>	<b>92.1</b>	<u>77.9</u>	<u>56.0</u>	<b>53.6</b>	<b>36.6</b>
	AnomalyCLIP	84.0	95.3	86.4	86.1	76.9	49.1	47.9	31.5
	AdaCLIP	<u>97.3</u>	<u>99.2</u>	<u>95.3</u>	<u>91.8</u>	38.7	<b>61.8</b>	33.0	19.7
	HeadCLIP	93.8	98.3	92.6	90.8	<b>80.8</b>	54.9	<u>51.4</u>	<u>34.6</u>
cable	AnoVL	<b>86.1</b>	<b>90.8</b>	<b>84.3</b>	70.7	<b>69.1</b>	17.9	<u>27.0</u>	<u>15.6</u>
	AnomalyCLIP	65.2	77.6	77.9	67.2	51.4	5.6	10.8	5.7
	AdaCLIP	76.6	86.1	79.3	<u>82.2</u>	43.3	<b>24.6</b>	<b>28.8</b>	<b>16.8</b>
	HeadCLIP	<u>80.1</u>	<u>87.6</u>	<u>81.3</u>	<b>84.0</b>	<u>67.9</u>	<u>17.9</u>	23.7	13.4
capsule	AnoVL	70.9	91.6	<u>93.1</u>	86.9	59.9	8.4	15.2	8.2
	AnomalyCLIP	86.4	97.1	91.0	93.4	<b>89.5</b>	24.7	<u>28.6</u>	<u>16.7</u>
	AdaCLIP	<b>93.0</b>	<b>98.5</b>	<b>93.3</b>	<b>96.4</b>	27.8	<b>38.7</b>	19.6	10.9
	HeadCLIP	<u>88.6</u>	<u>97.6</u>	92.3	<u>95.1</u>	<u>88.8</u>	<u>26.4</u>	<b>30.2</b>	<b>17.8</b>
carpet	AnoVL	99.5	99.8	98.3	97.8	89.6	45.0	49.1	32.5
	AnomalyCLIP	<u>100.0</u>	<u>100.0</u>	<u>99.4</u>	98.8	<b>96.7</b>	<u>63.5</u>	<b>63.1</b>	<b>46.1</b>
	AdaCLIP	<b>100.0</b>	<b>100.0</b>	<b>100.0</b>	<u>98.9</u>	55.9	<b>65.1</b>	26.7	15.4
	HeadCLIP	<b>100.0</b>	<b>100.0</b>	<b>100.0</b>	<b>98.9</b>	<u>93.7</u>	63.0	<u>61.7</u>	<u>44.6</u>
grid	AnoVL	<b>99.9</b>	<b>100.0</b>	<b>99.1</b>	<u>96.1</u>	<b>88.5</b>	15.2	23.3	13.2
	AnomalyCLIP	96.2	98.7	<u>94.4</u>	93.2	<u>79.7</u>	23.3	<u>32.4</u>	<u>19.3</u>
	AdaCLIP	<u>99.8</u>	<u>99.9</u>	<b>99.1</b>	92.4	3.2	<u>29.6</u>	5.0	2.6
	HeadCLIP	96.9	99.0	<u>94.4</u>	<b>97.8</b>	58.9	<b>31.5</b>	<b>35.3</b>	<b>21.4</b>
hazelnut	AnoVL	91.4	95.6	87.9	94.7	78.5	29.6	36.0	22.0
	AnomalyCLIP	<u>95.2</u>	<b>97.7</b>	<b>92.9</b>	<u>96.7</u>	<b>94.8</b>	<u>48.4</u>	<u>49.5</u>	<u>32.9</u>
	AdaCLIP	<b>95.3</b>	<u>97.5</u>	<u>92.1</u>	<b>97.6</b>	67.2	<b>57.1</b>	<b>54.0</b>	<b>37.0</b>
	HeadCLIP	91.0	95.3	88.3	96.6	<u>89.6</u>	46.1	46.4	30.2
leather	AnoVL	<b>100.0</b>	<b>100.0</b>	<b>100.0</b>	98.9	<u>95.3</u>	33.8	37.3	22.9
	AnomalyCLIP	<u>99.8</u>	<u>99.9</u>	98.9	99.0	<b>97.1</b>	35.3	37.6	23.1
	AdaCLIP	99.8	99.9	<u>99.5</u>	<u>99.3</u>	53.7	<b>57.4</b>	<u>38.9</u>	<u>24.2</u>
	HeadCLIP	<b>100.0</b>	<b>100.0</b>	<b>100.0</b>	<b>99.3</b>	94.6	<u>47.1</u>	<b>48.1</b>	<b>31.6</b>
metal nut	AnoVL	<u>93.3</u>	<u>98.5</u>	<u>93.0</u>	71.4	52.5	21.6	29.7	17.5
	AnomalyCLIP	90.7	97.7	92.9	<b>80.2</b>	<u>72.7</u>	<u>30.9</u>	<b>36.7</b>	<b>22.5</b>
	AdaCLIP	78.4	95.3	89.4	68.6	39.5	22.1	21.0	11.7
	HeadCLIP	<b>95.5</b>	<b>98.9</b>	<b>96.3</b>	<u>78.8</u>	<b>75.9</b>	<b>32.1</b>	<u>35.2</u>	<u>21.3</u>
pill	AnoVL	83.8	96.6	91.6	80.8	72.5	15.0	20.5	11.4
	AnomalyCLIP	77.5	94.0	92.4	<u>89.6</u>	<u>90.2</u>	<u>26.4</u>	<u>29.4</u>	<u>17.2</u>
	AdaCLIP	<b>91.8</b>	<b>98.3</b>	<b>94.7</b>	<b>91.7</b>	35.5	<b>33.8</b>	16.9	9.2
	HeadCLIP	<u>85.4</u>	<u>96.7</u>	<u>93.3</u>	85.9	<b>91.4</b>	26.3	<b>29.7</b>	<b>17.4</b>
screw	AnoVL	76.4	91.2	86.3	91.3	64.9	5.8	13.5	7.2
	AnomalyCLIP	<u>87.8</u>	<b>95.6</b>	<u>89.2</u>	<u>97.7</u>	<b>91.3</b>	<u>25.7</u>	<u>29.7</u>	<u>17.4</u>
	AdaCLIP	<b>89.1</b>	<u>95.6</u>	<b>91.9</b>	<b>98.7</b>	63.3	<b>37.0</b>	<b>41.9</b>	<b>26.5</b>
	HeadCLIP	82.0	93.0	88.8	96.6	<u>84.9</u>	19.8	25.0	14.3
tile	AnoVL	<u>100.0</u>	<u>100.0</u>	<u>99.4</u>	91.2	74.2	43.4	49.8	33.1
	AnomalyCLIP	<b>100.0</b>	<b>100.0</b>	<b>100.0</b>	<u>95.0</u>	<b>89.6</b>	<u>65.1</u>	<u>64.7</u>	<u>47.8</u>
	AdaCLIP	99.7	99.9	98.8	88.6	11.3	59.4	13.6	7.3
	HeadCLIP	99.6	99.9	98.8	<b>96.8</b>	<u>89.0</u>	<b>72.1</b>	<b>67.8</b>	<b>51.3</b>
toothbrush	AnoVL	<u>93.9</u>	<u>97.7</u>	<u>92.1</u>	92.6	<u>81.2</u>	13.3	23.5	13.3
	AnomalyCLIP	83.3	92.0	<u>92.1</u>	90.0	81.1	10.4	16.8	9.2
	AdaCLIP	90.8	96.6	89.6	<b>97.2</b>	59.3	<b>45.8</b>	<b>45.7</b>	<b>29.7</b>
	HeadCLIP	<b>99.2</b>	<b>99.7</b>	<b>98.3</b>	<u>95.6</u>	<b>93.5</b>	<u>36.1</u>	<u>39.8</u>	<u>24.8</u>
transistor	AnoVL	88.5	<u>87.9</u>	82.1	<b>73.8</b>	<u>54.9</u>	<b>22.0</b>	<b>30.2</b>	<b>17.8</b>
	AnomalyCLIP	<b>92.8</b>	<b>91.5</b>	<u>82.2</u>	65.1	<b>54.9</b>	13.1	16.4	8.9
	AdaCLIP	86.2	87.1	77.8	63.3	24.8	14.7	9.2	4.8
	HeadCLIP	<u>89.9</u>	86.7	<b>82.2</b>	<u>70.7</u>	54.6	15.5	<u>16.9</u>	<u>9.2</u>
wood	AnoVL	<u>97.4</u>	<u>99.2</u>	96.0	95.5	77.4	57.4	51.7	34.9
	AnomalyCLIP	96.9	99.2	<u>96.6</u>	<u>96.5</u>	<b>94.8</b>	<u>61.9</u>	<u>59.1</u>	<u>42.0</u>
	AdaCLIP	97.3	99.1	96.0	91.6	16.7	47.2	11.0	5.8
	HeadCLIP	<b>98.9</b>	<b>99.6</b>	<b>96.8</b>	<b>97.5</b>	<u>94.7</u>	<b>69.2</b>	<b>64.6</b>	<b>47.8</b>
zipper	AnoVL	93.5	98.2	92.8	94.7	<b>82.5</b>	24.9	<u>35.1</u>	<u>21.3</u>
	AnomalyCLIP	<u>97.8</u>	<u>99.4</u>	<u>97.1</u>	88.9	67.5	37.4	<b>43.8</b>	<b>28.1</b>
	AdaCLIP	<b>98.7</b>	<b>99.7</b>	97.0	<u>95.7</u>	2.6	<b>53.4</b>	5.3	2.7
	HeadCLIP	97.5	99.3	<b>97.9</b>	<b>95.7</b>	<u>74.4</u>	<u>41.1</u>	33.5	20.1

Table 10: ZSAD performance comparison on MVTecAD. Best performance shown in **bold**, second-best shown in underline. For image-level, R, A, F denote AUROC, AP, F1-max; for pixel-level, R, P, A, F, I denote AUROC, AUPRO, AP, F1-max, IoU-max respectively.

Subclass	Model	Image-level			Pixel-level				
		R	A	F	R	P	A	F	I
candle	AnoVL	<u>94.7</u>	<u>95.3</u>	<b>90.7</b>	95.1	82.9	6.6	13.9	7.5
	AnomalyCLIP	67.8	71.7	68.1	98.3	<u>96.2</u>	<u>27.0</u>	<b>38.2</b>	<b>23.6</b>
	AdaCLIP	<b>95.7</b>	<b>96.3</b>	<u>90.4</u>	<b>99.0</b>	48.0	<b>32.8</b>	33.7	20.3
	HeadCLIP	84.8	87.1	78.4	<u>98.8</u>	<b>96.6</b>	23.8	<u>37.5</u>	<u>23.1</u>
capsules	AnoVL	76.5	84.9	81.4	84.8	46.2	2.7	8.7	4.5
	AnomalyCLIP	<u>83.0</u>	<u>89.6</u>	<u>84.2</u>	94.4	<u>87.9</u>	16.5	24.3	13.8
	AdaCLIP	80.5	88.5	80.4	<b>98.3</b>	51.2	<b>43.0</b>	<b>49.4</b>	<b>32.8</b>
	HeadCLIP	<b>94.6</b>	<b>97.0</b>	<b>90.6</b>	<u>96.4</u>	<b>90.9</b>	<u>34.4</u>	<u>42.8</u>	<u>27.2</u>
cashew	AnoVL	<u>89.9</u>	95.4	<u>87.8</u>	89.4	85.7	6.9	9.7	5.1
	AnomalyCLIP	81.2	91.4	82.3	89.1	<u>90.6</u>	15.8	<u>20.3</u>	<u>11.3</u>
	AdaCLIP	<b>90.3</b>	<b>95.8</b>	<b>88.6</b>	<u>93.8</u>	43.1	<u>27.6</u>	17.6	9.6
	HeadCLIP	89.0	<u>95.4</u>	86.3	<b>96.7</b>	<b>94.9</b>	<b>35.6</b>	<b>40.2</b>	<b>25.2</b>
chewinggum	AnoVL	95.8	98.0	91.4	96.6	74.6	45.3	50.2	33.5
	AnomalyCLIP	97.1	98.7	94.5	<u>99.5</u>	<u>93.9</u>	<u>77.9</u>	<u>72.4</u>	<u>56.7</u>
	AdaCLIP	<u>97.1</u>	<u>98.8</u>	<u>95.4</u>	<b>99.6</b>	46.7	<b>84.3</b>	<b>76.7</b>	<b>62.2</b>
	HeadCLIP	<b>97.9</b>	<b>99.2</b>	<b>96.9</b>	99.4	<b>94.3</b>	61.9	65.1	48.3
fryum	AnoVL	87.7	94.0	86.6	86.6	68.2	19.2	<u>29.3</u>	<u>17.2</u>
	AnomalyCLIP	88.5	94.5	86.5	92.8	<b>86.2</b>	18.3	23.8	13.5
	AdaCLIP	<u>91.1</u>	<u>96.0</u>	<u>89.4</u>	<u>93.1</u>	31.6	<u>21.3</u>	12.0	6.4
	HeadCLIP	<b>91.7</b>	<b>96.1</b>	<b>90.4</b>	<b>94.6</b>	<u>84.6</u>	<b>27.6</b>	<b>33.4</b>	<b>20.1</b>
macaroni1	AnoVL	68.6	71.0	70.4	85.6	55.1	0.2	1.2	0.6
	AnomalyCLIP	82.3	81.2	<u>78.8</u>	98.7	<b>93.7</b>	<u>21.0</u>	<u>30.4</u>	<u>17.9</u>
	AdaCLIP	<u>83.6</u>	<u>84.0</u>	78.5	<b>99.3</b>	43.5	<b>22.1</b>	<b>30.7</b>	<b>18.1</b>
	HeadCLIP	<b>87.5</b>	<b>87.9</b>	<b>82.0</b>	<u>98.8</u>	<u>93.0</u>	11.2	21.1	11.8
macaroni2	AnoVL	64.9	64.1	<u>68.3</u>	80.6	41.1	0.1	0.2	0.1
	AnomalyCLIP	<u>67.9</u>	<u>65.5</u>	68.0	98.3	<u>87.6</u>	1.9	4.7	2.4
	AdaCLIP	58.9	61.9	67.3	<b>98.7</b>	49.6	<b>9.3</b>	<b>16.7</b>	<b>9.1</b>
	HeadCLIP	<b>71.3</b>	<b>69.1</b>	<b>71.9</b>	<u>98.4</u>	<b>88.3</b>	<u>4.1</u>	<u>8.4</u>	<u>4.4</u>
pcb1	AnoVL	77.9	78.1	77.7	<b>94.3</b>	76.0	<b>13.7</b>	<b>25.9</b>	<b>14.9</b>
	AnomalyCLIP	83.6	84.5	78.3	87.2	<u>78.7</u>	4.5	8.6	4.5
	AdaCLIP	<b>85.7</b>	<b>86.9</b>	<b>80.0</b>	92.1	40.2	5.7	10.1	5.3
	HeadCLIP	<u>85.2</u>	<u>85.7</u>	<u>79.1</u>	<u>92.7</u>	<b>84.6</b>	<u>6.3</u>	<u>10.3</u>	<u>5.4</u>
pcb2	AnoVL	48.0	46.5	68.1	87.6	59.6	1.3	3.4	1.7
	AnomalyCLIP	63.1	64.1	68.7	<u>91.1</u>	<u>76.1</u>	8.0	16.0	8.7
	AdaCLIP	<b>75.1</b>	<b>75.8</b>	<b>74.2</b>	90.7	46.6	<b>18.2</b>	<b>28.9</b>	<b>16.9</b>
	HeadCLIP	<u>70.1</u>	<u>71.3</u>	<u>71.3</u>	<b>92.1</b>	<b>80.7</b>	<u>9.2</u>	<u>16.6</u>	<u>9.0</u>
pcb3	AnoVL	63.6	62.4	67.4	78.2	39.1	0.6	1.3	0.6
	AnomalyCLIP	67.8	73.0	67.4	<u>89.7</u>	<u>74.0</u>	5.5	9.7	5.1
	AdaCLIP	<b>78.7</b>	<b>82.7</b>	<b>75.0</b>	<b>90.1</b>	42.1	<b>25.1</b>	<b>31.9</b>	<b>19.0</b>
	HeadCLIP	<u>69.3</u>	<u>74.5</u>	<u>67.7</u>	89.7	<b>78.3</b>	<u>11.3</u>	<u>19.8</u>	<u>11.0</u>
pcb4	AnoVL	75.0	74.0	72.8	93.0	<u>78.0</u>	23.3	<u>31.1</u>	<u>18.4</u>
	AnomalyCLIP	94.2	94.7	87.2	92.7	77.6	17.0	23.8	13.5
	AdaCLIP	<u>95.9</u>	<u>96.3</u>	<u>90.9</u>	<b>96.0</b>	63.8	<b>36.3</b>	<b>40.1</b>	<b>25.1</b>
	HeadCLIP	<b>97.3</b>	<b>97.1</b>	<b>92.8</b>	<u>94.2</u>	<b>84.0</b>	<u>24.1</u>	30.0	17.6
pipe fryum	AnoVL	79.1	89.3	82.7	86.3	89.5	5.8	12.0	6.4
	AnomalyCLIP	<u>94.2</u>	<u>97.4</u>	<u>91.5</u>	<u>96.7</u>	<b>95.9</b>	<u>28.9</u>	<u>36.4</u>	<u>22.3</u>
	AdaCLIP	92.5	96.4	88.8	95.8	73.3	24.0	24.9	14.2
	HeadCLIP	<b>96.5</b>	<b>98.4</b>	<b>93.6</b>	<b>97.3</b>	<u>95.5</u>	<b>31.2</b>	<b>41.8</b>	<b>26.4</b>

Table 11: ZSAD performance comparison on VisA. Best performance shown in **bold**, second-best shown in underline. For image-level, R, A, F denote AUROC, AP, F1-max; for pixel-level, R, P, A, F, I denote AUROC, AUPRO, AP, F1-max, IoU-max respectively.

Subclass	Model	Image-level			Pixel-level				
		R	A	F	R	P	A	F	I
bracket black	AnoVL	42.8	55.6	74.6	32.4	2.4	0.1	0.2	0.1
	AnomalyCLIP	49.7	58.7	75.2	<b>96.4</b>	<b>89.0</b>	<b>8.7</b>	<b>16.4</b>	<b>8.9</b>
	AdaCLIP	<b>72.2</b>	<b>78.0</b>	<b>78.3</b>	94.6	33.3	4.8	12.2	6.5
	HeadCLIP	<u>61.2</u>	<u>65.4</u>	<u>76.7</u>	<u>95.6</u>	<u>87.1</u>	<u>4.9</u>	<u>13.1</u>	<u>7.0</u>
bracket brown	AnoVL	45.2	67.8	79.7	31.5	3.7	0.3	0.9	0.5
	AnomalyCLIP	<b>64.7</b>	<b>80.5</b>	<u>81.0</u>	93.8	<b>90.3</b>	<u>4.7</u>	9.4	4.9
	AdaCLIP	52.9	71.5	80.3	<b>94.3</b>	17.3	<b>6.0</b>	<b>11.0</b>	<b>5.8</b>
	HeadCLIP	<u>62.2</u>	<u>75.4</u>	<b>81.3</b>	<u>93.9</u>	<u>84.7</u>	<u>4.7</u>	<u>9.4</u>	<u>4.9</u>
bracket white	AnoVL	40.9	53.4	67.4	58.4	12.0	0.0	0.1	0.1
	AnomalyCLIP	70.7	<b>76.1</b>	69.8	<b>99.8</b>	<u>97.7</u>	<b>16.9</b>	<b>26.8</b>	<b>15.5</b>
	AdaCLIP	<b>76.3</b>	<u>75.5</u>	<b>78.9</b>	98.1	14.3	1.3	3.5	1.8
	HeadCLIP	<u>72.4</u>	68.7	<u>76.2</u>	<u>99.6</u>	<b>97.8</b>	<u>16.3</u>	<u>26.6</u>	<u>15.3</u>
connector	AnoVL	77.9	62.3	64.9	78.6	38.1	1.4	3.2	1.6
	AnomalyCLIP	<b>86.9</b>	<b>76.8</b>	<b>72.7</b>	95.0	<b>83.8</b>	14.9	20.2	11.2
	AdaCLIP	74.8	63.9	62.9	<b>97.2</b>	46.4	<b>41.1</b>	<b>42.0</b>	<b>26.6</b>
	HeadCLIP	<u>78.6</u>	<u>70.9</u>	<u>66.7</u>	<u>95.1</u>	<u>83.3</u>	<u>21.9</u>	<u>25.4</u>	<u>14.6</u>
metal plate	AnoVL	<b>97.2</b>	<b>98.9</b>	<b>96.6</b>	<b>95.5</b>	<u>85.5</u>	<b>69.0</b>	<b>68.5</b>	<b>52.1</b>
	AnomalyCLIP	69.3	88.7	84.5	94.6	<b>87.6</b>	<u>63.4</u>	<u>64.5</u>	<u>47.6</u>
	AdaCLIP	84.0	94.3	87.6	<u>95.0</u>	38.4	62.2	36.2	22.1
	HeadCLIP	<u>94.6</u>	<u>97.9</u>	<u>93.8</u>	92.2	83.2	60.4	56.6	39.5
tubes	AnoVL	86.3	93.7	86.8	93.2	75.5	11.7	17.7	9.7
	AnomalyCLIP	95.4	97.9	<u>92.8</u>	97.1	<u>90.1</u>	32.0	33.4	20.1
	AdaCLIP	<b>99.6</b>	<b>99.8</b>	<b>97.9</b>	<b>99.1</b>	70.4	<b>71.2</b>	<b>66.8</b>	<b>50.2</b>
	HeadCLIP	<u>95.6</u>	<u>98.0</u>	92.1	<u>97.7</u>	<b>91.3</b>	<u>47.4</u>	<u>47.1</u>	<u>30.8</u>

Table 12: ZSAD performance comparison on MPDD. Best performance shown in **bold**, second-best shown in underline. For image-level, R, A, F denote AUROC, AP, F1-max; for pixel-level, R, P, A, F, I denote AUROC, AUPRO, AP, F1-max, IoU-max respectively.

Subclass	Model	Image-level			Pixel-level				
		R	A	F	R	P	A	F	I
01	AnoVL	89.5	96.3	89.9	<u>94.0</u>	<u>58.7</u>	<u>41.8</u>	<u>47.4</u>	<u>31.1</u>
	AnomalyCLIP	<u>96.3</u>	<u>98.6</u>	<u>93.6</u>	84.3	47.7	21.9	25.6	14.7
	AdaCLIP	52.8	80.8	82.4	83.9	5.9	39.9	16.5	9.0
	HeadCLIP	<b>96.7</b>	<b>98.9</b>	<b>96.8</b>	<b>94.2</b>	<b>79.1</b>	<b>54.4</b>	<b>58.1</b>	<b>40.9</b>
02	AnoVL	59.6	92.1	93.0	79.2	26.5	24.3	31.7	18.8
	AnomalyCLIP	81.2	96.9	<u>93.2</u>	94.8	<u>69.8</u>	65.1	<u>62.3</u>	<u>45.3</u>
	AdaCLIP	<u>84.4</u>	<u>97.4</u>	<b>94.3</b>	<b>96.6</b>	43.0	<b>71.4</b>	35.7	21.7
	HeadCLIP	<b>88.0</b>	<b>98.1</b>	<u>93.2</u>	<u>95.9</u>	<b>72.8</b>	<u>69.8</u>	<b>66.0</b>	<b>49.3</b>
03	AnoVL	66.8	16.3	25.0	86.1	69.1	3.8	9.3	4.9
	AnomalyCLIP	83.8	51.4	50.7	93.5	<u>86.1</u>	6.5	14.1	7.6
	AdaCLIP	<u>98.0</u>	<u>91.4</u>	<u>87.2</u>	<u>95.4</u>	28.4	<b>28.0</b>	<b>29.6</b>	<b>17.4</b>
	HeadCLIP	<b>98.9</b>	<b>94.6</b>	<b>91.6</b>	<b>96.6</b>	<b>92.2</b>	<u>18.8</u>	<u>28.5</u>	<u>16.6</u>

Table 13: ZSAD performance comparison on BTAD. Best performance shown in **bold**, second-best shown in underline. For image-level, R, A, F denote AUROC, AP, F1-max; for pixel-level, R, P, A, F, I denote AUROC, AUPRO, AP, F1-max, IoU-max respectively.

Subclass	Model	Image-level			Pixel-level				
		R	A	F	R	P	A	F	I
electrical commutators	AnoVL	83.2	76.9	67.2	<u>86.5</u>	51.9	18.7	27.5	15.9
	AnomalyCLIP	<b>85.4</b>	<b>80.8</b>	<u>74.0</u>	82.1	<u>53.0</u>	<u>28.1</u>	<u>35.5</u>	<u>21.6</u>
	AdaCLIP	75.8	60.7	57.1	73.9	5.9	21.4	7.0	3.6
	HeadCLIP	<u>84.6</u>	<u>77.2</u>	<b>74.2</b>	<b>91.3</b>	<b>65.6</b>	<b>40.7</b>	<b>43.3</b>	<b>27.6</b>

Table 14: ZSAD performance comparison on SDD. Best performance shown in **bold**, second-best shown in underline. For image-level, R, A, F denote AUROC, AP, F1-max; for pixel-level, R, P, A, F, I denote AUROC, AUPRO, AP, F1-max, IoU-max respectively.

Subclass	Model	Image-level			Pixel-level				
		R	A	F	R	P	A	F	I
Class1	AnoVL	60.8	20.1	29.9	66.7	27.4	1.1	3.3	1.7
	AnomalyCLIP	84.4	47.7	53.8	86.1	<u>73.9</u>	36.0	<u>41.3</u>	<u>26.0</u>
	AdaCLIP	<u>94.9</u>	<u>77.7</u>	<u>71.5</u>	<u>86.9</u>	24.2	<u>47.0</u>	21.1	11.8
	HeadCLIP	<b>97.6</b>	<b>89.8</b>	<b>82.1</b>	<b>89.6</b>	<b>79.0</b>	<b>53.0</b>	<b>55.9</b>	<b>38.8</b>
Class2	AnoVL	99.5	98.2	95.7	96.5	89.6	15.9	27.4	15.9
	AnomalyCLIP	<u>100.0</u>	<u>99.9</u>	<u>99.4</u>	<u>99.2</u>	<u>98.8</u>	<b>72.1</b>	<b>67.6</b>	<b>51.1</b>
	AdaCLIP	<u>100.0</u>	99.9	98.8	97.6	31.0	66.6	27.8	16.2
	HeadCLIP	<b>100.0</b>	<b>100.0</b>	<b>100.0</b>	<b>99.6</b>	<b>98.8</b>	<u>71.4</u>	<u>67.5</u>	<u>51.0</u>
Class3	AnoVL	98.9	96.1	93.3	93.8	80.4	8.9	16.9	9.2
	AnomalyCLIP	99.8	99.2	96.4	91.9	<u>88.5</u>	61.3	<u>64.8</u>	<u>48.0</u>
	AdaCLIP	<u>100.0</u>	<u>100.0</u>	<u>98.8</u>	<u>94.9</u>	25.9	<u>69.7</u>	27.8	16.2
	HeadCLIP	<b>100.0</b>	<b>100.0</b>	<b>100.0</b>	<b>95.7</b>	<b>93.5</b>	<b>71.0</b>	<b>70.3</b>	<b>54.2</b>
Class4	AnoVL	94.1	83.9	76.1	86.3	<u>70.0</u>	<b>8.8</b>	<b>16.8</b>	<b>9.2</b>
	AnomalyCLIP	<u>97.1</u>	<u>89.6</u>	<u>83.7</u>	85.7	65.9	4.0	12.0	6.4
	AdaCLIP	91.9	73.3	67.1	<u>89.3</u>	0.5	3.2	0.8	0.4
	HeadCLIP	<b>98.0</b>	<b>92.5</b>	<b>88.4</b>	<b>91.1</b>	<b>77.0</b>	<u>6.8</u>	<u>16.5</u>	<u>9.0</u>
Class5	AnoVL	<u>95.4</u>	88.0	<u>82.7</u>	91.3	72.1	14.2	20.1	11.2
	AnomalyCLIP	<b>100.0</b>	<b>100.0</b>	<b>100.0</b>	95.5	<u>88.2</u>	61.6	<u>63.0</u>	<u>46.0</u>
	AdaCLIP	<b>100.0</b>	<b>100.0</b>	<b>100.0</b>	<u>98.3</u>	34.8	<b>80.8</b>	39.2	24.4
	HeadCLIP	<b>100.0</b>	<b>100.0</b>	<b>100.0</b>	<b>98.9</b>	<b>96.4</b>	<u>75.8</u>	<b>73.4</b>	<b>58.0</b>
Class6	AnoVL	99.8	98.7	94.2	95.2	85.0	42.5	46.5	30.3
	AnomalyCLIP	<b>100.0</b>	<b>100.0</b>	<b>100.0</b>	96.4	<u>90.8</u>	75.5	<u>74.4</u>	<u>59.3</u>
	AdaCLIP	<b>100.0</b>	<b>100.0</b>	<b>100.0</b>	<u>98.7</u>	41.5	<b>85.5</b>	49.5	32.9
	HeadCLIP	<b>100.0</b>	<b>100.0</b>	<b>100.0</b>	<b>99.4</b>	<b>96.9</b>	<u>85.1</u>	<b>78.8</b>	<b>65.1</b>
Class7	AnoVL	85.6	56.2	55.3	75.6	47.7	4.9	10.2	5.4
	AnomalyCLIP	99.9	99.5	96.9	89.7	<u>83.9</u>	59.1	<u>63.9</u>	<u>47.0</u>
	AdaCLIP	<b>100.0</b>	<b>100.0</b>	<b>100.0</b>	<b>94.3</b>	51.5	<b>75.8</b>	56.2	39.1
	HeadCLIP	<u>100.0</u>	<u>99.9</u>	<u>98.7</u>	<u>90.8</u>	<b>87.2</b>	<u>64.3</u>	<b>66.8</b>	<b>50.1</b>
Class8	AnoVL	72.7	38.3	38.7	73.2	33.9	0.3	1.6	0.8
	AnomalyCLIP	94.9	87.9	82.7	95.6	<u>92.3</u>	52.1	<u>56.1</u>	<u>39.0</u>
	AdaCLIP	<b>99.7</b>	<b>98.2</b>	<b>96.3</b>	<u>97.3</u>	14.4	<b>64.0</b>	18.6	10.3
	HeadCLIP	<u>97.5</u>	<u>92.8</u>	<u>87.5</u>	<b>98.4</b>	<b>98.0</b>	<u>62.7</u>	<b>62.8</b>	<b>45.8</b>
Class9	AnoVL	94.3	77.5	69.8	96.1	87.4	2.6	7.5	3.9
	AnomalyCLIP	98.0	93.5	86.8	97.6	<u>93.2</u>	42.4	<u>46.1</u>	<u>29.9</u>
	AdaCLIP	<b>99.8</b>	<b>99.0</b>	<b>96.3</b>	<u>97.8</u>	43.0	<b>66.8</b>	27.1	15.7
	HeadCLIP	<u>99.1</u>	<u>94.0</u>	<u>88.7</u>	<b>99.7</b>	<b>98.8</b>	<u>50.0</u>	<b>50.6</b>	<b>33.8</b>
Class10	AnoVL	98.0	93.5	90.7	<u>98.7</u>	96.1	19.9	28.7	16.8
	AnomalyCLIP	99.9	99.3	<u>97.3</u>	98.2	<u>96.7</u>	<u>66.8</u>	<u>64.8</u>	<u>47.9</u>
	AdaCLIP	<u>99.9</u>	<u>99.5</u>	96.7	97.9	18.8	56.5	11.0	5.8
	HeadCLIP	<b>100.0</b>	<b>100.0</b>	<b>100.0</b>	<b>99.2</b>	<b>98.4</b>	<b>70.3</b>	<b>67.8</b>	<b>51.3</b>

Table 15: ZSAD performance comparison on DAGM. Best performance shown in **bold**, second-best shown in underline. For image-level, R, A, F denote AUROC, AP, F1-max; for pixel-level, R, P, A, F, I denote AUROC, AUPRO, AP, F1-max, IoU-max respectively.

Subclass	Model	Image-level			Pixel-level				
		R	A	F	R	P	A	F	I
Blotchy 099	AnoVL	98.3	99.6	98.1	98.4	93.5	50.1	48.1	31.7
	AnomalyCLIP	97.9	99.4	98.1	<u>99.6</u>	<b>97.6</b>	81.8	<u>76.0</u>	<u>61.3</u>
	AdaCLIP	<b>100.0</b>	<b>100.0</b>	<b>100.0</b>	99.6	57.7	<u>82.1</u>	70.2	54.1
	HeadCLIP	<u>99.8</u>	<u>99.9</u>	<u>99.4</u>	<b>99.7</b>	<u>96.8</u>	<b>83.8</b>	<b>76.2</b>	<b>61.5</b>
Fibrous 183	AnoVL	96.8	99.2	95.1	97.9	92.1	38.9	46.4	30.2
	AnomalyCLIP	98.2	99.6	97.4	99.5	<u>98.7</u>	<u>81.0</u>	<u>75.3</u>	<u>60.4</u>
	AdaCLIP	<u>99.0</u>	<u>99.8</u>	<u>98.1</u>	<u>99.5</u>	85.3	80.0	72.8	57.3
	HeadCLIP	<b>99.6</b>	<b>99.9</b>	<b>98.1</b>	<b>99.7</b>	<b>98.7</b>	<b>84.6</b>	<b>77.5</b>	<b>63.2</b>
Marbled 078	AnoVL	97.4	99.4	96.8	98.3	93.7	46.8	50.0	33.3
	AnomalyCLIP	98.6	99.7	97.4	99.3	<u>98.0</u>	<u>77.7</u>	<b>70.6</b>	<b>54.5</b>
	AdaCLIP	<u>98.9</u>	<u>99.8</u>	<u>98.1</u>	<b>99.6</b>	67.9	<b>84.5</b>	<u>69.7</u>	<u>53.5</u>
	HeadCLIP	<b>99.9</b>	<b>100.0</b>	<b>99.4</b>	<u>99.5</u>	<b>98.2</b>	74.8	69.0	52.7
Matted 069	AnoVL	<b>95.4</b>	<u>98.9</u>	<b>94.9</b>	96.7	77.3	25.2	31.8	18.9
	AnomalyCLIP	80.9	94.7	90.6	99.3	<u>84.3</u>	74.4	<u>68.6</u>	<u>52.2</u>
	AdaCLIP	<u>95.1</u>	<b>98.9</b>	<u>94.7</u>	<u>99.3</u>	70.4	<u>76.7</u>	68.2	51.7
	HeadCLIP	94.6	98.7	93.3	<b>99.7</b>	<b>87.5</b>	<b>79.6</b>	<b>72.2</b>	<b>56.5</b>
Mesh 114	AnoVL	79.9	91.8	83.7	88.8	64.3	23.6	31.0	18.3
	AnomalyCLIP	80.2	92.0	83.3	<b>96.7</b>	<b>87.9</b>	60.5	<u>60.1</u>	<u>42.9</u>
	AdaCLIP	<u>87.9</u>	<u>95.2</u>	<b>87.6</b>	95.1	36.4	<b>67.5</b>	52.7	35.8
	HeadCLIP	<b>88.1</b>	<b>95.3</b>	<u>86.4</u>	<u>96.1</u>	<u>82.1</u>	<u>61.6</u>	<b>61.1</b>	<b>44.0</b>
Perforated 037	AnoVL	<b>99.1</b>	<b>99.8</b>	<b>97.4</b>	<b>98.9</b>	<b>96.1</b>	46.2	47.6	31.2
	AnomalyCLIP	88.6	96.7	93.4	<u>96.9</u>	91.4	<u>66.8</u>	<b>65.8</b>	<b>49.0</b>
	AdaCLIP	<u>93.5</u>	<u>98.5</u>	93.5	96.1	22.0	66.7	31.2	18.5
	HeadCLIP	92.9	98.2	93.8	96.0	<u>92.5</u>	<b>67.3</b>	<u>64.3</u>	<u>47.4</u>
Stratified 154	AnoVL	<u>98.8</u>	<u>99.7</u>	97.5	99.3	<u>94.7</u>	68.1	61.6	44.5
	AnomalyCLIP	98.2	99.6	96.8	99.5	<b>98.9</b>	<b>81.3</b>	<b>73.7</b>	<b>58.4</b>
	AdaCLIP	<b>99.6</b>	<b>99.9</b>	<b>98.8</b>	99.1	40.4	77.2	27.2	15.8
	HeadCLIP	98.7	99.7	<u>98.1</u>	<b>99.7</b>	92.0	<u>78.4</u>	<u>72.3</u>	<u>56.6</u>
Woven 001	AnoVL	<u>94.8</u>	<u>98.0</u>	<u>92.8</u>	96.1	79.7	27.9	34.5	20.8
	AnomalyCLIP	<b>100.0</b>	<b>100.0</b>	<b>100.0</b>	99.7	<b>99.1</b>	<u>77.8</u>	<u>74.8</u>	<u>59.8</u>
	AdaCLIP	<b>100.0</b>	<b>100.0</b>	<b>100.0</b>	<b>99.8</b>	75.0	<b>85.0</b>	<b>76.1</b>	<b>61.5</b>
	HeadCLIP	<b>100.0</b>	<b>100.0</b>	<b>100.0</b>	<u>99.8</u>	<u>98.2</u>	74.7	69.6	53.4
Woven 068	AnoVL	89.0	93.7	85.5	97.8	90.9	27.6	36.2	22.1
	AnomalyCLIP	<u>96.9</u>	<u>98.4</u>	<u>94.9</u>	<u>98.9</u>	<u>96.0</u>	<u>62.1</u>	<u>58.8</u>	<u>41.6</u>
	AdaCLIP	<b>97.0</b>	<b>98.5</b>	<b>96.2</b>	98.5	69.8	<b>74.5</b>	<b>67.2</b>	<b>50.6</b>
	HeadCLIP	96.5	98.1	92.7	<b>99.2</b>	<b>96.8</b>	59.6	57.4	40.3
Woven 104	AnoVL	96.0	99.0	95.2	98.0	92.7	45.3	43.9	28.1
	AnomalyCLIP	<u>97.7</u>	<u>99.5</u>	<u>97.4</u>	96.5	<u>93.3</u>	68.4	<u>65.3</u>	<u>48.4</u>
	AdaCLIP	97.6	99.4	96.2	<b>98.3</b>	49.9	<b>74.5</b>	55.1	38.0
	HeadCLIP	<b>99.5</b>	<b>99.9</b>	<b>98.7</b>	<u>98.2</u>	<b>95.5</b>	<u>73.6</u>	<b>66.6</b>	<b>50.0</b>
Woven 125	AnoVL	96.5	99.2	96.1	97.3	91.8	31.0	39.2	24.4
	AnomalyCLIP	<u>99.7</u>	<u>99.9</u>	<u>98.7</u>	99.6	<b>98.5</b>	<u>80.7</u>	<b>72.9</b>	<b>57.4</b>
	AdaCLIP	<b>100.0</b>	<b>100.0</b>	<b>100.0</b>	<b>99.8</b>	66.3	<b>88.5</b>	71.1	55.1
	HeadCLIP	<b>100.0</b>	<b>100.0</b>	<b>100.0</b>	<u>99.6</u>	<u>98.1</u>	77.3	<u>71.7</u>	<u>55.9</u>
Woven 127	AnoVL	83.1	84.4	79.3	89.7	77.0	12.8	21.1	11.8
	AnomalyCLIP	79.2	83.1	75.5	94.3	<u>87.7</u>	48.6	<u>52.4</u>	<u>35.5</u>
	AdaCLIP	<u>88.3</u>	<u>89.2</u>	<u>84.5</u>	<u>94.6</u>	55.5	<b>61.8</b>	51.4	34.6
	HeadCLIP	<b>93.8</b>	<b>95.4</b>	<b>88.0</b>	<b>95.6</b>	<b>92.0</b>	<u>56.0</u>	<b>55.9</b>	<b>38.8</b>

Table 16: ZSAD performance comparison on DTD-Synthetic. Best performance shown in **bold**, second-best shown in underline. For image-level, R, A, F denote AUROC, AP, F1-max; for pixel-level, R, P, A, F, I denote AUROC, AUPRO, AP, F1-max, IoU-max respectively.

Subclass	Model	Pixel-level				
		R	P	A	F	I
skin	AnoVL	<b>93.3</b>	<b>84.0</b>	<b>84.7</b>	<b>77.4</b>	<b>63.1</b>
	AnomalyCLIP	<u>90.6</u>	81.5	<u>79.1</u>	<u>72.9</u>	<u>57.3</u>
	AdaCLIP	88.3	31.0	76.5	44.0	28.2
	HeadCLIP	90.1	<u>81.7</u>	78.8	72.1	56.4

Table 17: ZSAD performance comparison on ISIC. Best performance shown in **bold**, second-best shown in underline. For image-level, R, A, F denote AUROC, AP, F1-max; for pixel-level, R, P, A, F, I denote AUROC, AUPRO, AP, F1-max, IoU-max respectively.

Subclass	Model	Pixel-level				
		R	P	A	F	I
colon	AnoVL	77.6	47.9	20.9	28.8	16.8
	AnomalyCLIP	<u>81.6</u>	<u>69.1</u>	<u>25.6</u>	<u>34.1</u>	<u>20.6</u>
	AdaCLIP	80.8	44.9	24.3	27.8	16.1
	HeadCLIP	<b>83.8</b>	<b>72.8</b>	<b>30.3</b>	<b>37.1</b>	<b>22.7</b>

Table 18: ZSAD performance comparison on CVC-ColonDB. Best performance shown in **bold**, second-best shown in underline. For image-level, R, A, F denote AUROC, AP, F1-max; for pixel-level, R, P, A, F, I denote AUROC, AUPRO, AP, F1-max, IoU-max respectively.

Subclass	Model	Pixel-level				
		R	P	A	F	I
colon	AnoVL	80.9	53.2	<u>32.6</u>	37.1	22.7
	AnomalyCLIP	<u>82.5</u>	<u>65.8</u>	31.6	<u>39.3</u>	<u>24.4</u>
	AdaCLIP	77.0	26.5	27.3	25.9	14.9
	HeadCLIP	<b>85.6</b>	<b>71.0</b>	<b>38.1</b>	<b>44.2</b>	<b>28.4</b>

Table 19: ZSAD performance comparison on CVC-ClinicDB. Best performance shown in **bold**, second-best shown in underline. For image-level, R, A, F denote AUROC, AP, F1-max; for pixel-level, R, P, A, F, I denote AUROC, AUPRO, AP, F1-max, IoU-max respectively.

Subclass	Model	Pixel-level				
		R	P	A	F	I
colon	AnoVL	73.3	26.6	32.3	38.7	24.0
	AnomalyCLIP	<u>79.0</u>	<b>50.5</b>	<u>38.4</u>	<u>45.4</u>	<u>29.4</u>
	AdaCLIP	76.4	40.1	32.5	33.9	20.4
	HeadCLIP	<b>82.8</b>	<u>48.0</u>	<b>43.2</b>	<b>50.0</b>	<b>33.3</b>

Table 20: ZSAD performance comparison on Kvasir. Best performance shown in **bold**, second-best shown in underline. For image-level, R, A, F denote AUROC, AP, F1-max; for pixel-level, R, P, A, F, I denote AUROC, AUPRO, AP, F1-max, IoU-max respectively.

Subclass	Model	Pixel-level				
		R	P	A	F	I
colon	AnoVL	81.2	47.8	38.8	45.1	29.1
	AnomalyCLIP	<u>82.9</u>	<u>60.2</u>	<u>42.6</u>	<u>47.6</u>	<u>31.2</u>
	AdaCLIP	81.6	44.2	38.2	38.1	23.5
	HeadCLIP	<b>86.1</b>	<b>66.8</b>	<b>48.1</b>	<b>52.2</b>	<b>35.3</b>

Table 21: ZSAD performance comparison on Endo. Best performance shown in **bold**, second-best shown in underline. For image-level, R, A, F denote AUROC, AP, F1-max; for pixel-level, R, P, A, F, I denote AUROC, AUPRO, AP, F1-max, IoU-max respectively.

Subclass	Model	Pixel-level				
		R	P	A	F	I
thyroid	AnoVL	75.0	38.6	29.2	36.5	22.3
	AnomalyCLIP	76.8	<u>45.2</u>	38.7	<u>40.5</u>	<u>25.4</u>
	AdaCLIP	<u>80.6</u>	17.0	<u>42.9</u>	29.2	17.1
	HeadCLIP	<b>80.9</b>	<b>46.4</b>	<b>44.3</b>	<b>45.9</b>	<b>29.8</b>

Table 22: ZSAD performance comparison on TN3K. Best performance shown in **bold**, second-best shown in underline. For image-level, R, A, F denote AUROC, AP, F1-max; for pixel-level, R, P, A, F, I denote AUROC, AUPRO, AP, F1-max, IoU-max respectively.

Subclass	Model	Image-level		
		R	A	F
brain	AnoVL	85.1	84.8	79.0
	AnomalyCLIP	91.8	91.5	87.9
	AdaCLIP	<u>94.7</u>	<u>93.7</u>	<u>89.4</u>
	HeadCLIP	<b>95.2</b>	<b>95.9</b>	<b>91.5</b>

Table 23: ZSAD performance comparison on HeadCT. Best performance shown in **bold**, second-best shown in underline. For image-level, R, A, F denote AUROC, AP, F1-max; for pixel-level, R, P, A, F, I denote AUROC, AUPRO, AP, F1-max, IoU-max respectively.

Subclass	Model	Image-level		
		R	A	F
brain	AnoVL	85.2	90.4	83.8
	AnomalyCLIP	92.3	94.1	89.9
	AdaCLIP	<b>96.5</b>	<b>97.6</b>	<b>94.3</b>
	HeadCLIP	<u>96.1</u>	<u>96.5</u>	<u>93.8</u>

Table 24: ZSAD performance comparison on BrainMRI. Best performance shown in **bold**, second-best shown in underline. For image-level, R, A, F denote AUROC, AP, F1-max; for pixel-level, R, P, A, F, I denote AUROC, AUPRO, AP, F1-max, IoU-max respectively.



Subclass	Model	Image-level		
		R	A	F
brain	AnoVL	82.7	83.4	77.4
	AnomalyCLIP	94.1	94.4	86.9
	AdaCLIP	<b>98.0</b>	<b>98.1</b>	<u>92.2</u>
	HeadCLIP	<u>97.9</u>	<u>97.9</u>	<b>93.3</b>

Table 25: ZSAD performance comparison on Br35H. Best performance shown in **bold**, second-best shown in underline. For image-level, R, A, F denote AUROC, AP, F1-max; for pixel-level, R, P, A, F, I denote AUROC, AUPRO, AP, F1-max, IoU-max respectively.

Subclass	Model	Image-level		
		R	A	F
chest	AnoVL	64.2	44.1	42.4
	AnomalyCLIP	<u>79.3</u>	<u>53.4</u>	<u>53.6</u>
	AdaCLIP	70.8	48.4	49.0
	HeadCLIP	<b>86.5</b>	<b>59.2</b>	<b>56.4</b>

Table 26: ZSAD performance comparison on COVID-19. Best performance shown in **bold**, second-best shown in underline. For image-level, R, A, F denote AUROC, AP, F1-max; for pixel-level, R, P, A, F, I denote AUROC, AUPRO, AP, F1-max, IoU-max respectively.